UNIVERSITY OF CALIFORNIA,
IRVINE

Numerical Analysis of Breakup of Electrified Jets

THESIS

submitted in partial satisfaction of the requirements
for the degree of

MASTER OF SCIENCE

in Mechanical and Aerospace Engineering

by

Kaartikey Misra

Thesis Committee:
Professor Manuel Gamero-Castaño, Chair
Professor William A. Sirignano
Professor Roger Rangel

2023

TABLE OF CONTENTS

Page

LIST OF FIGURES **iii**

LIST OF ALGORITHMS **v**

ACKNOWLEDGMENTS **v**

ABSTRACT OF THE THESIS **vi**

1 Introduction **1**
- 1.1 Overview . . . 1
- 1.2 Background . . . 2
- 1.3 Motivation . . . 5

2 Theoretical Analysis and Numerical Model **7**
- 2.1 Linear Stability Analysis . . . 7
- 2.2 Non-Linear Model Formulation . . . 12
- 2.3 Connection Between the Breakup Model and Cone-Jets of Highly Conducting Liquids . . . 19

3 Model Validation **21**

4 Role of Oh and Γ on Jet Breakup **27**
- 4.1 Jet Breakup with Low Viscous Effect . . . 27
- 4.2 Jet Breakup with High Viscous Effect . . . 33
- 4.3 Droplet Stability Criteria . . . 39
- 4.4 Jets with maximum growth rates . . . 40

5 Conclusions and Future Work **44**
- 5.1 Conclusions . . . 44
- 5.2 Future Work . . . 46

Bibliography **47**

Appendix A Role of outer electrode and charge conservation **51**

LIST OF FIGURES

Page

1.1 Schematic depicting electrospray operating in cone-jet mode 2

2.1 Linear stability analysis trends for the growth rate (s) with dimensionless wave-number kRj for three different viscosity levels $Oh^2 = 0.1, 1, 10$ and under different levels of electrification $\Gamma = 0, 0.3, 0.6$ and 0.9 11
2.2 Schematic of the problem and computational domain. 13

3.1 a) Evolution of the jet for $Oh = 0.079$, $\Gamma = 0.9$ and $k = 0.7$, the axial axis is normalized by λ; b) radii of primary and satellite droplets, comparison between the solution of the phase field model (PF) and the experimental and numerical data (LHGC) of López-Herrera and Gañán-Calvo [1] for $Oh = 0.079$, $\Gamma = 0.9$; c) charge of primary droplets; and d) charge of satellite droplets. Charges are normalized with the charge of the droplet at the Rayleigh limit. 22
3.2 a) Evolution of the jet for $Oh = 0.271$, $\Gamma = 0.9$ and $k = 0.7$, the axial axis is normalized by λ; b) radii of primary and satellite droplets, comparison between the solution of the phase field model (PF) and the experimental and numerical data (LHGC) of López-Herrera and Gañán-Calvo [1] for $Oh = 0.271$, $\Gamma = 0.9$; c) charge of primary droplets (PD); d) charge of "Satellite Droplet" SD; (e) radius of the satellite (S) and sub-satellite (S1) droplets; and (f) charge of the satellite (S) and sub-satellite (S1) droplets. Charges are normalized with the charge of the droplet at the Rayleigh limit. 24
3.3 Experimental images obtained by López-Herrera and Gañán-Calvo [1] for $Oh = 0.271$ and $\Gamma = 0.9$ showing (a) The primary and satellite droplets; (b) 1-4 different stages of the breakup of satellite droplet "SD" (figure reproduced with permission, © 2004 Cambridge University Press) 25

4.1 Evolution of breakups with small viscous effects, $Oh = 0.1$, for two wavenumbers $k = 0.5$ and $k = 0.8$, and several electrification levels: a) $\Gamma = 0$; b) $\Gamma = 1$; c) $\Gamma = 2$; and d) $\Gamma = 3$. 28
4.2 Results of the phase field model for breakups with small viscous effects, $Oh = 0.1$, as a function of the Taylor number and wavenumber: a) time at first pinch-off; b) radius of primary droplets; c) radius of S and $S1$ satellite droplets; d) charge of the primary droplet relative to its Rayleigh limit; (e) charge of the S and $S1$ satellite droplets relative to their Rayleigh limit; (f) fraction of the total charge carried by the satellite droplets. 30

4.3 Electric potential map and radial velocity, axial velocity, potential and normal component of the electric field on the surface, for $Oh = 0.1$, $\Gamma = 2$ and $k = 0.7$: a) solution at $t = 13.7$ coinciding with zero radial velocity at $z = \lambda/2$; b) solution just before pinch-off. c) Electric potential maps before ($t = 16.6$), near ($t = 16.95$), and after ($t = 17.9$) the second pinch-off. The last inset shows the maxima of the electric field. 32
4.4 Retracting thread and sub-satellite formation process for $k = 0.5$, $\Gamma = 2$ and $Oh = 0.1$ 33
4.5 Evolution of breakups with high viscous effects, $Oh = 10$, for two wavenumbers $k = 0.5$ and $k = 0.8$, and several electrification levels: a) $\Gamma = 0$; b) $\Gamma = 1$; c) $\Gamma = 2$; and d) $\Gamma = 3$. 34
4.6 Results of the phase field model for breakups with high viscous effects, $Oh = 10$, as a function of the Taylor number and wavenumber: a) time at first pinch-off; b) radius of primary droplets; c) radius of S and $S1$ satellite droplets; d) charge of the primary droplet relative to its Rayleigh limit; (e) charge of the S and $S1$ satellite droplets relative to their Rayleigh limit; (f) fraction of the total charge carried by the satellite droplets. 36
4.7 Electric potential map and radial velocity, axial velocity, potential and normal component of the electric field on the surface, for $Oh = 10$, $\Gamma = 2$ and $k = 0.7$: a) solution at $t = 453$ coinciding with zero radial velocity at $z = \lambda/2$; and b) solution just before pinch-off. c) Electric potential maps before ($t = 538$), at ($t = 554$), and after ($t = 568$) second pinch-off. The last inset shows the location and values of electric field maxima. 37
4.8 Formation of sub-satellite droplet from the retracting slender thread for $Oh = 10$, $\Gamma = 2$ and $k = 0.5$. $z/\lambda = 0$ depicts the primary droplet location and $z/\lambda = 0.5$ depicts the location of the satellite droplet. 38
4.9 (a) Charge of the primary droplet (PD) and; (b) charge of satellite droplet (S) with respect to Rayleigh charge limit for different k, Oh and Γ values. . . 40
4.10 Droplet radius (predicted from the associated critical wavenumber (k^*) as a function of the Taylor number obtained with linear stability theory. Comparison with two wavenumbers of fastest pinch-off (phase field model), and the radius $R^{I_B}_{Ray}$ of the droplet charged at the Rayleigh limit and having the jet's charge-to-mass ratio. 41
4.11 Phase field model prediction for wavenumbers associated with maximum growth-rate for different Taylor numbers- (a) normalized radius of the primary droplet along with the modal radius suggested by linear stability analysis, (b) normalized radius of satellite (S) and sub-satellite droplet (S1), (c) dimensionless charge carried by primary and satellite droplet, (d) fraction of total charge carried by the satellite droplet. 42

ACKNOWLEDGMENTS

I would first like to thank my committee chair Dr. Manuel Gamero-Castaño for giving me an opportunity to pursue my graduate studies under his supervision along with providing me with all the guidance and motivation along the journey. His stimulating weekly discussions along with constructive criticisms have helped me mature as an academic. I would also like to thank my committee members Dr. William A. Sirignano and Dr. Roger Rangel for their time and effort into reading this thesis. I would also like to thank the suggestions by anonymous referees of the original draft of the article, parts of which are reprinted in the thesis.

I would also like to thank my lab mates: Dr. Albert, Dr. Marco, Marc and Manel for creating an intellectually stimulating environment both during and after work hours. Finally I would like to thank my family, my girlfriend and friends for their encouragement during the low days.

Lastly, I want to acknowledge the Science and Engineering Research Board (SERB), DST, India for the financial support during my graduate studies along with the American Physical Society for granting me the permission to reuse our work published in Physical Review Fluids in this thesis.

The text of this thesis is a reprint of the material as it appears in ("Leaky-dielectric phase field model for the axisymmetric breakup of an electrified jet", K. Misra M. Gamero-Castaño, Physical Review Fluids, 7, 064004 (2022)), used with permission from American Physical society.

ABSTRACT OF THE THESIS

Numerical Analysis of Breakup of Electrified Jets

By

Kaartikey Misra

Master of Science in Mechanical and Aerospace Engineering

University of California, Irvine, 2023

Professor Manuel Gamero-Castaño, Chair

The natural instability and breakup of electrified cone jets leads to the formation of charged droplets with size and charge distribution of the droplets governed by the physical properties and electrospraying conditions under consideration. This thesis develops a leaky-dielectric model to study the axisymmetric breakup of an electrified jet, using the phase field method to treat interfacial phenomena. The model is used to analyze the breakup in a wide range of the Taylor number (Γ), the Ohnesorge number (Oh) and the wavenumber relevant to electrosprays operating in the cone-jet mode. The phase field technique accurately captures the behavior of the jet after pinch-off and predicts the formation of primary and satellite droplets. The numerical results are compared with existing experimental and numerical studies, extending them to account for the formation of sub-satellite droplets. It is found that for highly viscous jets, $Oh \gg 1$, the number of sub-satellite droplets generated increases with the Taylor number when compared to low viscous jets, hence widening the size distribution of droplets. At fixed Γ and Oh the primary droplets are charged to an approximately constant ratio of the Rayleigh charge limit, regardless of the wave number. Furthermore, the primary droplets are charged below the Rayleigh limit for $\Gamma \lesssim 1.5$, and charged above the Rayleigh limit when $\Gamma \gtrsim 1.5$. Thus, most primary droplets are expected to be unstable at Taylor numbers exceeding 1.5.

Chapter 1

Introduction

1.1 Overview

Electrosprays operating in the cone-jet mode [1, 2, 3] are characterized by the emission of a stationary and long jet from the vertex of a liquid meniscus, resulting from the interplay between an imposed electric field, the fluid dynamics of the liquid, and its surface tension. The natural instability of the jet is suppressed by the accelerating effect of the electric field, but once the latter becomes sufficiently weak away from the vertex, the jet becomes unstable and breaks into charged droplets [4, 5]. The axisymmetric breakup of the stationary jet produces droplets characterized by a narrow distribution of diameters with an average that depends on the physical properties of the liquid and its flow rate. Figure 1.1 depicts this description. Various technological applications benefit from such fine sprays (for a detailed review see Gañán-Calvo et al. [6], Rosell-Llompart et al. [7]), making the study of the breakup not only of fundamental but also of practical interest.

Depending on the properties of the working fluid, the radius of the cone-jets can vary anywhere from $5 - 10\mu m$ down to $10nm$. Therefore, a direct experimental measurement for the

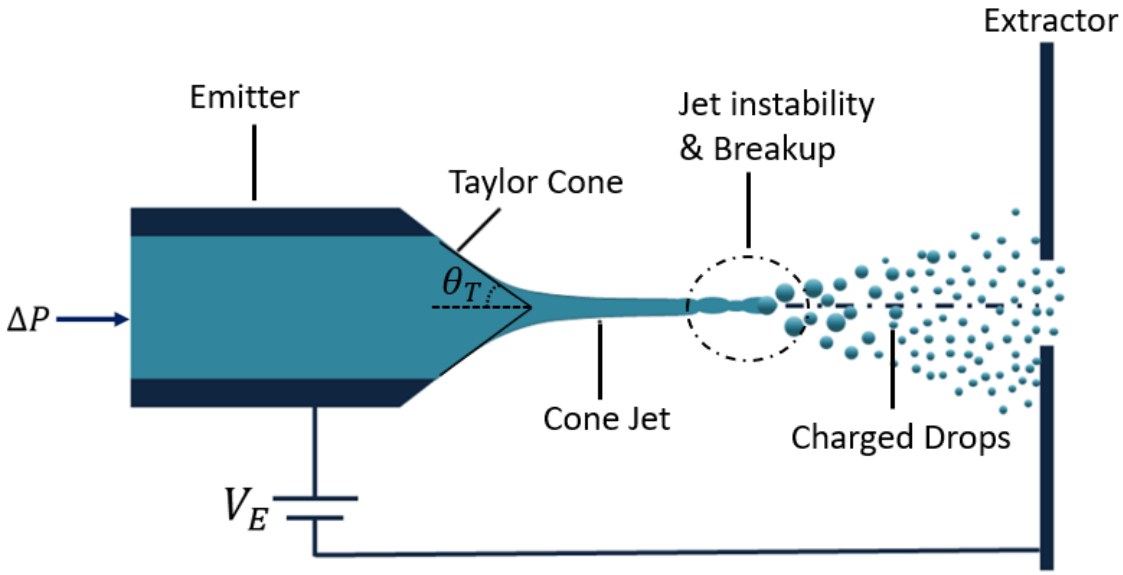

Figure 1.1: Schematic depicting electrospray operating in cone-jet mode

size distribution of charged droplets is usually not possible. Moreover, accurately simulating the entire cone jet electrospray process (i.e. formation of Taylor cone, ejection of jet followed by the formation of charged droplets) is usually cost consuming due to the different orders of magnitude of length scale involved in the physics. Therefore, the problem of destabilization and breakup of electrified jets is usually studied either using linear stability analysis (small deformation), or a non-linear numerical approach (large deformation).

1.2 Background

Linear stability analyses consider an infinitely long cylindrical jet of radius R_j, and impose a sinusoidal perturbation on the surface so that its position can be defined as $R = R_j(1 + \epsilon e^{st+ikz/R_j})$, where s is the growth rate of the perturbation, k its specified wavenumber, and ϵ an arbitrarily small number. The basic goal of the analysis is to find the range of wavenumbers for which the growth rate is positive, i.e. which make the jet unstable. Furthermore the wavenumber with fastest growth rate yields the diameter of the droplet most

likely to be produced by the breakup, or modal droplet. Basset [8] analyzed the breakup of an equipotential and inviscid jet subjected to axi-symmetric perturbations. Melcher [9] extended Basset's analysis by including both axisymmetric and non-axisymmetric perturbations. Saville [10] included viscosity into the equipotential problem, and found that when the viscosity is sufficiently high, the axisymmetric instability modes are damped and non-axisymmetric modes dominate, leading to jet whipping [10, 11]. Mestel [12, 13] relaxed the assumption of equipotential breakup and investigated the effect of surface charge and tangential electrical stresses. López-Herrera et al. [14] used linear stability analysis to study the deformation and breakup of jets with finite electrical conductivity, and the role of a downstream electrode. Wang [15] studied the breakup of jets with finite electrical conductivity using both linear stability and non-linear analysis for jets surrounded by another viscous medium in the Stokes limit.

Linear stability analysis can only probe the initial stages of the breakup, and the study of phenomena dependent on large deformation such as the generation of satellite droplets requires the use of non-linear numerical calculations. Setiawan and Heister [16] formulated a non-linear boundary element algorithm (BEM) to study the axisymmetric breakup of an inviscid and equipotential jet. They considered high electrification levels and observed the formation of satellite droplets along with primary droplets. They calculated pinch-off times and the sizes of primary and satellite droplets. López-Herrera et al. [17] extended the model of Lee [18] to study the breakup of a viscous and equipotential jet at low electrification levels and low-moderate viscosities. They calculated the sizes and charges of the primary and satellite droplets for different wavenumbers. The numerical results were found to be in good agreement with experimental data [1]. Collins et al. [19] studied the equipotential breakup of a jet subjected to a radial electric field, for wide ranges of electrification and viscosity levels. They showed that as the level of electrification increases, the size of the satellite droplet increases monotonically, thereby reducing the size of primary droplets. They also showed that for a fixed electrification level, the size of satellite droplets decreases as the viscosity

increases, a trend also observed in the experiments of López-Herrera and Gañán-Calvo [1]. For high electrification, the charges carried by primary and satellite droplets can exceed the Rayleigh [20] stability limit, leading to the possibility of the subsequent breakup of these droplets. Collins et al. [19] also showed that satellite droplets are produced for electrified jet's in the Stoke's limit. This feature is not observed in uncharged jets, but has been reported when the jet is surrounded by a viscous medium [21, 22]. Wang and Papageorgiou [23] studied the non-linear breakup of a perfect conducting viscous thread surrounded by another viscous medium at zero Reynolds number. Nie et al. [24] developed a leaky-dielectric electrohydrodynamic (EHD) model to study the role of different charge relaxation mechanisms on the pinch-off and formation of satellite droplets. A distinction must be made between the implementation of the equipotential condition by several authors. It is always possible to impose a constant potential on the surface of the jet, e.g. as in [19]. In this case the potential field inside the jet is constant and does not need to be resolved, but the total charge in the simulated section of the jet is not conserved. On the other hand, one can ensure quasi-equipotentiality by including a conservation of charge equation in the model, imposing an electric relaxation time much smaller than the breakup time, and solving for the potential inside the jet. This approach ensures conservation of charge and therefore is more physical. López-Herrera and Gañán-Calvo [1] and Li et al. [25] discuss in detail these two approaches.

Few non-linear models utilize the Volume of Fluid or the Level Set methods to study the deformation and breakup of electrified jets. These phase field methods are useful to reproduce the formation of additional sub-satellite droplets after the first pinch-off. Eck et al. [26] developed a phase field model for electrowetting. They coupled the Navier-Stokes equation and electrostatic charge transport equations with the Cahn-Hilliard phase field equations. For the EHD system in two and three dimensions, they proved the existence of weak solutions for the governing dynamics of electrowetting. Lakdawala et al. [27] formulated a dual grid level set method to study the breakup of conducting liquid threads of low viscosity and electrification level. They showed that, for sufficiently long perturbations, sub-satellite

droplets may also form along with the primary and satellite droplets. López-Herrera et al. [28] developed a volume of fluid model to study the role of electrokinetic effects on the deformation and breakup of conducting jets when the breakup time is comparable or smaller than the diffusion time scale.

1.3 Motivation

Existing non-linear analyses do not capture the liquid threads formed after pinch-off and which may generate sub-satellite droplets [19, 23, 29, 30]. Moreover, most existing non-linear analysis have imposed the constant-potential condition and usually study jets under low or moderate levels of electrification. Motivated by this and the recent experimental studies of cone-jets of liquids with high electrical conductivities [31, 32], the present article develops a phase field, leaky-dielectric EHD model to study the axisymmetric breakup of an electrified jet. The leaky dielectric model [33] uses a simplified electrokinetic approach that assumes a complete relaxation of free charges at the interface of the free surface, leading to a uniform electrical conductivity within the liquid bulk. Therefore, a key assumption made in the leaky dielectric model is the hydrodynamic time scales are much larger than the electric relaxation time. The model does not consider any potential variation in electrical conductivity within the liquid (which may be relevant at the pinch-off region of the jet) due to the leaky-dielectric nature of the model. The model does not consider the effect of an imposed axial electric field, which is negligible in the breakup region of most cone-jets [1, 17, 34, 35], and is not applicable to sinuous or whipping instabilities and ramified jet breakups [6, 36].

The remainder of the thesis is organized as follows: Chapter 2 presents the existing linear stability analysis results for electrified jet followed by the description of the non-linear model developed along with the numerical procedure, finally we establish the connection between

the sets of dimensionless numbers parametrizing the breakup and cone-jets. In Chapter 3 the numerical solution is validated with existing experimental and numerical results. In Chapter 4 the breakup of electrified jets is investigated for selected wavenumbers and broad ranges of the Ohnesorge and Taylor numbers. Concluding remarks and recommendations for the future work are presented in Chapter 5.

Chapter 2

Theoretical Analysis and Numerical Model

2.1 Linear Stability Analysis

As discussed in Chapter 1, linear stability analysis of electrified jets can probe the initial deformation stages of the jet, providing a range of wave-numbers (k) for which the jet is unstable (and the associated growth-rates). This information is valuable as the analysis can also predict the critical wavenumber (k^*) (hence the modal radius) of droplets with fastest growth rate (minimum breakup-time).

Here, we will summarize the linear stability analysis of viscous jets performed by Chandrasekhar [37] which was extended by Gamero-Castaño and Hurby [5] to account for surface charge, leading to electrostatic stresses. A cylindrical jet of radius R_j carrying a surface charge density ρ_{so} is slightly perturbed such that it's shape is given by:

$$S(z,t) = R_j(1 + \epsilon e^{st+ikz}) \tag{2.1}$$

The jet is assumed to be perfectly conducting, therefore, the surface of the jet can be approximated as an equipotential surface (i.e. no volumetric charge and electric field within the bulk of the jet). Therefore, the pressure (p), velocity (u_r, u_z), surface charge (ρ_s) and electric potential (V) distribution can be written as:

$$\begin{aligned} p &= p_o + \epsilon p_1(r)e^{st+ikz} + \mathcal{O}(\epsilon^2) \\ u_r &= \epsilon u_{1r}(r)e^{st+ikz} + \mathcal{O}(\epsilon^2) \\ u_z &= \epsilon u_{1z}(r)e^{st+ikz} + \mathcal{O}(\epsilon^2) \\ \rho_s &= \rho_{so} + \epsilon \rho_{s1} e^{st+ikz} + \mathcal{O}(\epsilon^2) \\ V &= V_o(r) + \epsilon V_1(r)e^{st+ikz} + \mathcal{O}(\epsilon^2) \end{aligned} \tag{2.2}$$

The continuity, momentum and Laplace equation for electrostatics accounting for the first-order term can be written as:

$$\begin{aligned} \frac{\partial u_{1r}}{\partial r} + \frac{\partial u_{1z}}{\partial z} &= 0 \\ \frac{\partial u_{1r}}{\partial t} &= -\frac{1}{\rho}\frac{\partial p_1}{\partial r} + \nu\left(\frac{1}{r}\frac{\partial}{\partial r}\left(r\frac{\partial u_{1r}}{\partial r}\right) + \frac{\partial^2 u_{1r}}{\partial z^2}\right) \\ \frac{\partial u_{1z}}{\partial t} &= -\frac{1}{\rho}\frac{\partial p_1}{\partial z} + \nu\left(\frac{1}{r}\frac{\partial}{\partial r}\left(r\frac{\partial u_{1z}}{\partial r}\right) + \frac{\partial^2 u_{1z}}{\partial z^2}\right) \\ \frac{1}{r}\frac{\partial}{\partial r}\left(r\frac{\partial V}{\partial r}\right) + \frac{\partial^2 V}{\partial z^2} &= 0 \end{aligned} \tag{2.3}$$

The jet surface is subjected to kinematic boundary condition for the radial velocity:

$$u_r(R_j) = \epsilon u_{1r}(R_j)e^{st+ikz} = \frac{D}{Dt}S(z,t) = \epsilon R_j s e^{st+ikz} + \mathcal{O}(\epsilon^2) \tag{2.4}$$

The tangential and normal stress balance at the jet interface ($r = S(z,t)$) contribute to two

additional boundary conditions:

$$\begin{aligned} \nu\rho(\frac{\partial u_r}{\partial z} + \frac{\partial u_z}{\partial r}) &= 0 \\ p + \frac{\rho_s^2}{2\varepsilon_o} - 2\nu\rho\frac{\partial u_r}{\partial r} &= \gamma(\frac{1}{R_1} + \frac{1}{R_2}) \end{aligned} \tag{2.5}$$

Since a perfectly conducting jet is considered, the tangential electrostatic stresses are absent as reflected in equation 2.5. Imposing a constant potential (zero for reference) at the jet surface gives:

$$V(R_j) = 0 \tag{2.6}$$

The solutions to continuity and momentum equations in 2.3 are given by (see Chandrasekhar [37]):

$$p_1 = A\rho R_j I_o(kr) \tag{2.7}$$

$$u_{1r}(r) = k[BI_1(r\sqrt{k^2 + \frac{s}{\nu}}) - \frac{AR_j}{s}I_1(kr)] \tag{2.8}$$

$$u_{1z}(r) = i[B\sqrt{k^2 + \frac{s}{\nu}}I_o(r\sqrt{k^2 + \frac{s}{\nu}}) - \frac{AR_j k}{s}I_o(kr)] \tag{2.9}$$

I_n is the modified Bessel function of first kind with order n, A and B are constants of integration. For the Laplace equation of electric potential, V_o is obtained by the potential variation for a perfectly conducting cylinder and imposing zero potential on jet surface, while $V_1(r)$ becomes the solution of Bessel equation (Gamero-Castaño and Hurby [5], Saville [10]):

$$V(r) = \frac{\rho_{so}}{\varepsilon_o} ln(\frac{r}{R_j}) + \epsilon \frac{\rho_{so}}{K_o(kR_j)\varepsilon_o} K_o(kr) e^{st+ikz} + \mathcal{O}(\epsilon^2) \tag{2.10}$$

K_n is the modified Bessel function of second kind with order n. From the electric potential solution, the volumetric charge density can be solved by using the condition that, for a cylindrical jet, $\rho_s = -\varepsilon_o \frac{\partial V}{\partial r}|_{r=R_j}$:

$$\rho_s = \rho_{so}(1 - \varepsilon[1 + \frac{kR_j K_o^{'}(kR_j)}{K_o(kR_j)}] e^{st+ikz}) + \mathcal{O}(\epsilon^2) \tag{2.11}$$

Using the solution for p, u_r and u_z for the tangential and normal stress balance (equation 2.5) we arrive at:

$$i\epsilon[BI_1(R_j(2k^2 + \frac{s}{\nu})\sqrt{k^2 + \frac{s}{\nu}}) - 2\frac{AR_j k^2}{s} I_1(kR_j)] e^{st+ikz} + \mathcal{O}(\epsilon^2) = 0 \tag{2.12}$$

$$\begin{aligned} \epsilon[A\rho R_j I_o(kR_j) + \frac{\rho_{so}\rho_{s1}}{\varepsilon_o} - 2\nu\rho k[B\sqrt{k^2 + \frac{s}{\nu}} I_o(R_j\sqrt{k^2 + \frac{s}{\nu}}) - \frac{AR_j k}{s} I_o(kR_j)] \\ +(1 - (kR_j^2))\frac{\gamma}{R_j}] e^{st+ikz} + (p_o + \frac{\rho_{so}^2}{2\varepsilon_o} - \frac{\gamma}{R_j}) + \mathcal{O}(\epsilon^2) = 0 \end{aligned} \tag{2.13}$$

Finally using the solutions given in equation (2.6), (2.7) and (2.8), the kinematic boundary condition for the velocity along the radial direction can be simplified:

$$\varepsilon k(BI_1(R_j\sqrt{k^2 + \frac{s}{\nu}}) - \frac{AR_j}{s} I_1(kR_j)) = \epsilon R_j s e^{st+ikz} + \mathcal{O}(\epsilon^2) \tag{2.14}$$

Finally, the set of equations (2.11, 2.12, 2.13 and 2.14) can be used to eliminate A, B, ρ_{s1}, to obtain the growth rate s as a function of wavenumber k. Using the definition $y = R_j\sqrt{k^2 + \frac{s}{\nu}}$ and $x = kR_j$, the growth rate can be estimated from (Gamero-Castaño and Hurby [5]):

$$\frac{sR_j}{\nu} = y^2 - x^2 \tag{2.15}$$

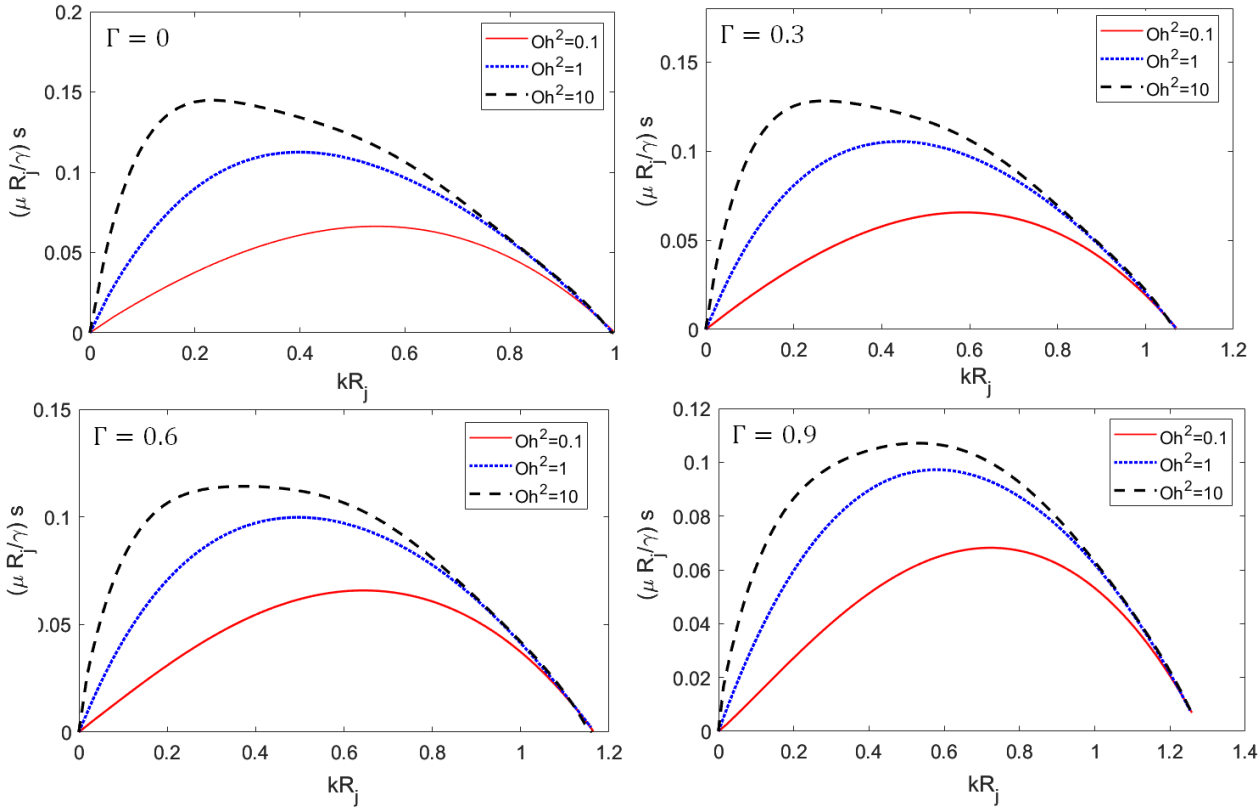

Figure 2.1: Linear stability analysis trends for the growth rate (s) with dimensionless wavenumber kRj for three different viscosity levels $Oh^2 = 0.1, 1, 10$ and under different levels of electrification $\Gamma = 0, 0.3, 0.6$ and 0.9

$$Oh^2[2x^2(x^2+y^2)\frac{I_1'(x)}{I_o(x)}[1-\frac{2xy}{x^2+y^2}\frac{I_1(x)I_1'(y)}{I_1'(x)I_1(y)}]-(x^4-y^4)] = x(1-x^2)\frac{I_1(x)}{I_o(x)}-\Gamma\frac{xI_1(x)}{I_o(x)}[1+\frac{xK_o'(x)}{K_o(x)}] \tag{2.16}$$

The Ohnesorge number $Oh = \mu/\sqrt{\gamma\rho R_j}$ is the ratio of between viscous time scale and inertial time scale. The Taylor umber $\Gamma = \varepsilon_o E_{no}^2 R_j/\gamma$ is the ratio between the normal electrostatic stress to the surface tension stress, where E_{no} is the outward normal electric field on the surface of the jet.

Figure 2.1 depicts the trends for growth rate for perfectly conducting jet as a function of the wavenumbers. For uncharged jets, $\Gamma = 0$, the maximum unstable wavenumber corresponds

to 1. Moreover, with increase in the electrification level of the jets, the jets are unstable over a wider range of wavenumbers, therefore promoting smaller droplet size distributions. Linear stability analysis also provides important detail about the maximum growth rate for a given Oh and Γ numbers, therefore, predicting the size of the droplet most likely to result from the natural breakup of the charged jet. The wavenumbers associated with maximum growth rate would be termed as critical wavenumbers (k^*). Highly viscous jets have much smaller critical wavenumbers when compared to jets with low viscous levels, therefore, suggesting the average size of droplets in highly viscous jets would be much larger than the droplets produced at low viscosity levels (considering same electrification level). Moreover, as the electrification level of the jet increases, the critical wavenumber also becomes larger, suggesting that the average size of droplets would be much smaller than uncharged jets. Chapter 4 will present an in-depth analysis of the critical wavenumbers and their comparison with the non-linear numerical model developed in the current thesis.

2.2 Non-Linear Model Formulation

For the numerical calculations, we assume a section of an infinitely long jet subjected to periodic perturbations. The rationale of using this simplified assumption is that since we consider only a section of real cone-jet, we use a periodic disturbance to a section of an infinitely long hypothetical jet to study the characteristics and dynamics of the breakup of the jet and formation of droplets (see Collins et al. [19]). Figure 2.2 depicts the schematic of the problem, modeled in cylindrical $\{z, r\}$ coordinates. The domain contains a liquid jet of length λ (Fluid 2), separated from a surrounding liquid (Fluid 1) by an interface $r = S(z, t)$. Fluid 1 is further enclosed by a cylindrical electrode of radius R_e. In its unperturbed state the jet has a radius R_j and a net charge q distributed homogeneously on its surface, inducing a normal electric field E_{no}

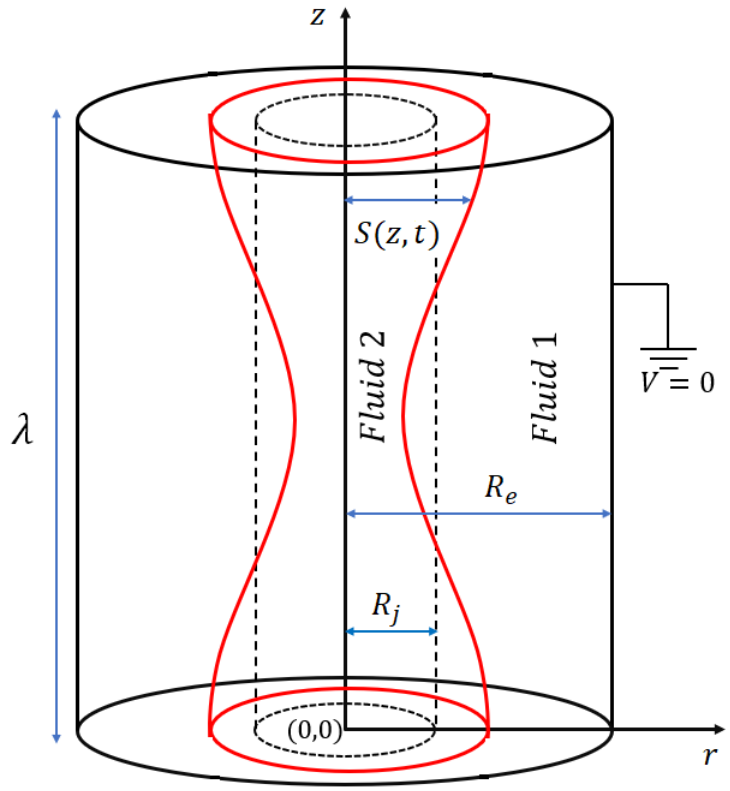

Figure 2.2: Schematic of the problem and computational domain.

$$E_{no} = \frac{q}{2\pi\varepsilon_0 R_j \lambda}. \tag{2.17}$$

To study the stability of the system a small sinusoidal perturbation is added to the position of the interface

$$S(z,0) = R_j\left(1 + A\,cos\frac{kz}{R_j}\right), \quad k = \frac{2\pi R_j}{\lambda} \tag{2.18}$$

In the numerical simulations we use $A = 0.015$ and $R_e = 12R_j$. The relevant physical properties of the fluids are the electrical conductivity K_i, relative permittivity ε_i, viscosity μ_i, and density ρ_i, as well as the surface tension γ of the interface. The subscript i indicates either Fluid 1 or 2.

The interface between the jet and the outer medium is modeled as a diffuse interface using

the phase field method [38]. A continuous phase variable ϕ is defined throughout the domain, varying from -1 to 1 between the bulks of Fluid 1 and Fluid 2 respectively, and fulfilling the Cahn-Hilliard equation [38, 39, 40]. The phase variable changes rapidly across the narrow, yet finite, thickness of the diffuse interface, so that the surface where $\phi = 0$ defines the mean interface $S(z,t)$. The physical properties are defined as continuous functions of ϕ throughout the domain. In particular, the density, the viscosity and the relative electrical permittivity are defined as the weighted arithmetic mean of ϕ, whereas the electrical conductivity is defined as its weighted harmonic mean [41, 42, 43]:

$$\rho = \rho_1(\frac{1-\phi}{2}) + \rho_2(\frac{1+\phi}{2}), \quad \mu = \mu_1(\frac{1-\phi}{2}) + \mu_2(\frac{1+\phi}{2}), \tag{2.19}$$

$$\varepsilon = \varepsilon_1(\frac{1-\phi}{2}) + \varepsilon_2(\frac{1+\phi}{2}), \quad \frac{1}{K} = \frac{1}{K_1}(\frac{1-\phi}{2}) + \frac{1}{K_2}(\frac{1+\phi}{2}). \tag{2.20}$$

Fluid 1 consists of vacuum space, i.e. μ_1 and ρ_1 are zero while $\varepsilon_1 = 1$; we set its electrical conductivity to a very small value, $K_1 = 10^{-12} S/m$. The model solves for the velocity $\boldsymbol{u}$, pressure p, and volumetric charge ρ_e, the electric potential V (the electric field is simply $\boldsymbol{E} = -\boldsymbol{\nabla} V$), and the phase field variable ϕ as functions of position and time. These field variables fulfill the equations of conservation of mass, momentum and charge, the Poisson equation, and the Cahn-Hilliard equation. They are written in dimensionless form using $l_c = R_j$, $t_c = \sqrt{\rho_2 R_j^3/\gamma}$, $v_c = l_c/t_c$, $p_c = \rho_2 v_c^2$, $E_c = E_{no}$, and $\rho_{e,c} = \varepsilon_0 E_{no}/R_j$ as the characteristic scales for length, time, velocity, pressure, electric field and volumetric charge respectively:

$$\boldsymbol{\nabla} \cdot \boldsymbol{u} = 0, \tag{2.21}$$

$$\frac{\partial(\frac{\rho}{\rho_2}\boldsymbol{u})}{\partial t} + \boldsymbol{\nabla}\cdot(\frac{\rho}{\rho_2}\boldsymbol{u}\boldsymbol{u}) = -\boldsymbol{\nabla}p + Oh\boldsymbol{\nabla}\cdot\frac{\mu}{\mu_2}(\boldsymbol{\nabla}\boldsymbol{u} + \boldsymbol{\nabla}\boldsymbol{u}^T) + \Gamma\boldsymbol{F}_{es} + \boldsymbol{F}_{st}, \tag{2.22}$$

$$\frac{\partial\rho_e}{\partial t} + \boldsymbol{\nabla}\cdot\rho_e\boldsymbol{u} = \frac{1}{\Pi_t}\boldsymbol{\nabla}\cdot\frac{K}{K_2}\boldsymbol{E}, \tag{2.23}$$

$$\nabla^2 V + \boldsymbol{\nabla}V\cdot\boldsymbol{\nabla}\varepsilon = -\rho_e, \tag{2.24}$$

$$\frac{\partial\phi}{\partial t} + \boldsymbol{u}\cdot\boldsymbol{\nabla}\phi = \frac{1}{Pe}\boldsymbol{\nabla}^2\psi, \quad \psi = \frac{1}{\xi}(\phi^2-1)\phi - \xi\nabla^2\phi, \tag{2.25}$$

where $\boldsymbol{F}_{es}$ is the electric body force [44]

$$\boldsymbol{F}_{es} = \boldsymbol{\nabla}\cdot\boldsymbol{T}_e = \boldsymbol{\nabla}\cdot\varepsilon(\boldsymbol{E}\boldsymbol{E} - \frac{1}{2}\boldsymbol{I}|E|^2) = \rho_e\boldsymbol{E} - \frac{1}{2}\boldsymbol{\nabla}\varepsilon\boldsymbol{E}\cdot\boldsymbol{E}, \tag{2.26}$$

and $\boldsymbol{F}_{st}$ is the surface tension body force [39, 40]

$$\boldsymbol{F}_{st} = \psi\boldsymbol{\nabla}\phi. \tag{2.27}$$

ξ in the Cahn-Hilliard equation (2.25) is the dimensionless interface thickness parameter, which provides a measure of the sharpness of the interface. In the sharp interface limit, the diffuse interface thickness goes to zero. In practice, the phase variable and the velocity are independent of the thickness parameter when the latter is sufficiently small, $\xi \lesssim 0.01 - 0.03$ [39].

Equations (2.21)-(2.27) include five dimensionless numbers: Oh, Γ, Π_t, Pe and the relative permittivity of the jet ε_2. The Ohnesorge number is the ratio between the viscous time scale

$t_\mu = \mu_2 R_j/\gamma$, and the characteristic time scale t_c

$$Oh = \frac{\mu_2}{\sqrt{\gamma \rho_2 R_j}}, \tag{2.28}$$

and measures the relative importance of viscous and capillary stresses. The Taylor number measures the relative importance between the electrostatic and capillary stresses

$$\Gamma = \frac{\varepsilon_o E_{no}^2 R_j}{\gamma}. \tag{2.29}$$

$\Gamma = 2$ indicates that the capillary and electrostatic stresses fully balance each other in the baseline jet, i.e. the pressure jump across the jet's surface is zero. Π_t is the ratio between the characteristic time scale and the electrical relaxation time of Fluid 2

$$\Pi_t = \frac{t_e}{t_c} = \frac{\varepsilon_o/K_2}{\sqrt{\rho_2 R_j^3/\gamma}}. \tag{2.30}$$

Π_t is indicative of the speed with which the charge in the bulk of Fluid 2 migrates to the surface as the jet deforms. Finally, the Peclet number measures the advection rate to the diffusion rate in the Cahn-Hilliard equation:

$$Pe = \frac{R_j^3}{\varsigma \gamma t_c}. \tag{2.31}$$

ς is the mobility parameter which we treat as a constant, such that for all the numerical cases considered in the current study $\varsigma = (R_j\xi)^2/p_c t_c$ [45, 46]. Therefore, alternatively we can define $Pe = 1/\xi^2$.

The problem is axisymmetric and since we consider an infinitely long jet, we apply periodic boundary conditions at $z = 0$ and $z = \lambda$. The boundary conditions for the electrical,

hydrodynamic and phase field problems are:

$$\boldsymbol{e}_z \cdot \boldsymbol{E}(r,0,t) = 0, \quad \boldsymbol{e}_z \cdot \boldsymbol{E}(r,\lambda,t) = 0, \quad V(R_e,z,t) = 0, \tag{2.32}$$

$$\boldsymbol{e}_z \cdot \boldsymbol{u}(r,0,t) = 0, \quad \boldsymbol{e}_z \cdot \boldsymbol{u}(r,\lambda,t) = 0, \quad \boldsymbol{u}(R_e,z,t) = 0 \tag{2.33}$$

$$\frac{\partial(\boldsymbol{e}_r \cdot \boldsymbol{u}(r,0,t))}{\partial z} = 0, \quad \frac{\partial(\boldsymbol{e}_r \cdot \boldsymbol{u}(r,\lambda,t))}{\partial z} = 0, \tag{2.34}$$

$$\boldsymbol{e}_z \cdot \boldsymbol{\nabla}\psi = \boldsymbol{e}_z \cdot \boldsymbol{\nabla}\phi = 0 \quad at\ z = 0,\ \lambda, \qquad \boldsymbol{e}_r \cdot \boldsymbol{\nabla}\psi = \boldsymbol{e}_r \cdot \boldsymbol{\nabla}\phi = 0, \quad at\ r = 0, \tag{2.35}$$

Along the symmetry axis ($r = 0$) the boundary conditions are:

$$\boldsymbol{e}_r \cdot \boldsymbol{u}(0,z,t) = \frac{\partial(\boldsymbol{e}_z \cdot \boldsymbol{u}(0,z,t))}{\partial r} = 0, \quad \boldsymbol{e}_r \cdot \boldsymbol{E} = 0, \quad \boldsymbol{e}_r \cdot \boldsymbol{\nabla}\psi = \boldsymbol{e}_r \cdot \boldsymbol{\nabla}\phi = 0 \tag{2.36}$$

$\boldsymbol{e}_r$ and $\boldsymbol{e}_z$ represent the unit vectors in the radial and the axial directions.

We solve the electro-hydrodynamic and phase field equations using the commercial COMSOL Multiphysics software. We use the built-in laminar flow, electrostatics and phase field interface, which uses a finite element solver in the weak form representation. The volumetric charge conservation equation cannot be incorporated with built-in interfaces, therefore, we manually define a weak form charge conservation equation using PDE interface. Additionally, we include the electrostatic (F_{es}) and surface tension (F_{st}) volumetric forces in the momentum equation as forcing terms. The equations are solved in COMSOL's weak formu-

lation framework. The phase variable ϕ is discretized using a cubic-order Lagrange element; $\boldsymbol{u}$, V and ρ_e are discretized using quadratic-order Lagrange elements; and p is discretized using a linear Lagrange element. We use the parallel sparse solver MUMPS for marching the solution in time. MUMPS uses a second-order backward differential formulation scheme with variable time step. The time stepping is computed using the Courant–Friedrichs–Lewy condition. When needed (e.g. to analyze the results), the position of the surface is computed as the loci where $\phi = 0$ by interpolation. For spatial discretization we use a triangular grid with grid size h.

Initially, a homogeneous volumetric charge $\rho_{eo} = 2$ in Fluid 2 is allowed to relax to the perturbed interface (2.18) by only solving the electric problem ($\boldsymbol{u} \equiv 0$). Once the charge is relaxed, the full set of equations is solved yielding the evolution of the jet and eventual breakup into droplets. The time-dependent simulations are solved using a parallel sparse direct solver, MUMPS with Backward Differential Formulation (BDF) for running the time stepping. In all simulations we use uniform meshing for the jet with node spacing h, such that $1/h = 33$. The thickness parameter for the phase field model is set such that $\xi = 0.5h$. We have verified that for $\xi = 1/100$ and $\xi = 1/66$, the numerical results are independent of the grid size. The simulations are done at fixed values of Π_t, Pe and ε_2, and varying the Taylor number, the Ohnesorge number, and the wavenumber to study the effects of these parameters. We set $\Pi_t = 0.02$ and $\varepsilon_2 = 12.2$, which are the values associated with the ionic liquid EMI-Im and whose cone-jets have been characterized in detail [31]; the small Π_t value is typical of cone-jets of highly conducting liquids, suggesting that under these electrospraying conditions the charge in the bulk rapidly relaxes to the surface and the breakup is quasi-equipotential. We set $Pe = 4356$, which is equivalent to using a thickness parameter $\xi = 1/66$. In Appendix A, we validate conservation of charge within the simulation domain while letting the jet deform and break into droplets. The maximum variation is within 1%-1.7% of the total charge.

2.3 Connection Between the Breakup Model and Cone-Jets of Highly Conducting Liquids

The solution of the breakup model is a function of Γ, Oh and Π_t. In order to apply the model to electrosprays, it is useful to express these dimensionless numbers in terms of those commonly used in the parametrization of cone-jets, namely the dimensionless flow rate Π_Q and the electric Reynolds number Re_K:

$$\Pi_Q = \frac{\rho_2 K_2 Q}{\gamma \varepsilon_0}, \tag{2.37}$$

$$Re_K = \left(\frac{\rho_2 \varepsilon_o \gamma^2}{\mu_2^3 K_2} \right)^{1/3}. \tag{2.38}$$

Re_K is a grouping of physical properties, while Π_Q also contains the flow rate Q. Both sets of dimensionless numbers can be related using well-established scaling laws for the electric current I of a cone-jet and the radius of the jet at the breakup [6]

$$I \cong \alpha \left(\gamma K_2 Q\right)^{1/2} = \alpha \left(\frac{\varepsilon_0 \gamma^2}{\rho_2} \right)^{1/2} {\Pi_Q}^{1/2}, \tag{2.39}$$

$$R_J \cong \beta \left(\frac{\rho_2 \varepsilon_o Q^3}{\gamma K_2} \right)^{1/6} = \beta \frac{\mu_2^2}{\rho_2 \gamma} {Re_K}^2 {\Pi_Q}^{1/2}, \tag{2.40}$$

and by noting that the dominant mechanism for charge transport in the jet is convection of the surface charge σ, which makes it possible to estimate the electric field normal to the surface of the jet

$$E_{no} = \frac{\sigma}{\varepsilon_o} = \frac{R_J I}{2 \varepsilon_o Q} \cong \frac{\alpha \beta}{2} \frac{{\rho_2}^{1/2} \gamma}{{\varepsilon_o}^{1/2} \mu_2} {Re_K}^{-1}. \tag{2.41}$$

The factors α and β are the dimensionless constants for the current and radius of the cone jet, respectively, which have been shown to be relatively insensitive to the operational conditions of electrosprays in the cone-jet mode (see for example [6]). The factor α is easily computed from experimental data: $\alpha = 2.6$ fits well data for many liquids in a wide range of operational conditions [6], and has been reproduced by numerical models [47]. The factor β is more difficult to obtain, because it requires measuring radii of jets that often are submicrometric. Recently, values for highly conducting liquids have been inferred [31, 32] using an experimental technique developed by Gamero-Castaño [48]. For example, $0.27 \leq \beta \leq 0.31$ in cone-jets of EMI-Im in the current range 230 nA $\leq I \leq$ 450 nA, at 21 ^{o}C emitter temperature [31]. Equations (2.28) - (2.30), (2.40) and (2.41) yield the relationship between the two sets of dimensionless numbers:

$$\Gamma \cong \frac{\alpha^2 \beta^3}{4} \Pi_Q^{1/2}, \tag{2.42}$$

$$Oh \cong \left(\beta \Pi_Q^{1/2} Re_K^2 \right)^{-1/2} \tag{2.43}$$

$$\Pi_t = \left(\beta \Pi_Q^{1/2} \right)^{-3/2}, \tag{2.44}$$

making it possible to estimate the ranges of Γ, Oh and Π_t of cone-jets.

Chapter 3

Model Validation

We validate the phase-field model with the numerical results and experiments reported by López-Herrera and Gañán-Calvo [1]. These authors measure the sizes and charges of primary and satellite droplets resulting from imposed axisymmetric perturbations with different wavenumbers, $0.5 < k < 0.9$, at moderate and small Taylor and Ohnesorge numbers, $\Gamma \leq 0.9$ and $Oh \leq 0.271$, and nearly equipotential conditions ($\Pi_t \sim 3 \times 10^{-5}$).

Figure 3.1 shows the solution of our model and the comparison with [1], for $Oh = 0.079$ and $\Gamma = 0.9$. Throughout the remainder of the thesis, we use the following nomenclature for the droplets: primary droplet, PD, refers to the larger droplets formed at $z = 0$ and $z = \lambda$; satellite droplet SD refers to the droplet that would contain the fluid and charge separated from the primary droplets by the initial pinch-off; this section of fluid may split into two or more droplets if there is a second pinch-off, producing a larger satellite droplet centered at $z = \lambda/2$ and referred to as S, and smaller sub-satellite droplets of decreasing size referred to as $S1$, $S2$ ... formed between the PD and the S droplets.

Figure 3.1(a) shows the evolution of the jet for $k = 0.7$, leading to the formation of a satellite droplet in addition to the primary droplet. The shape of the satellite droplet oscillates due

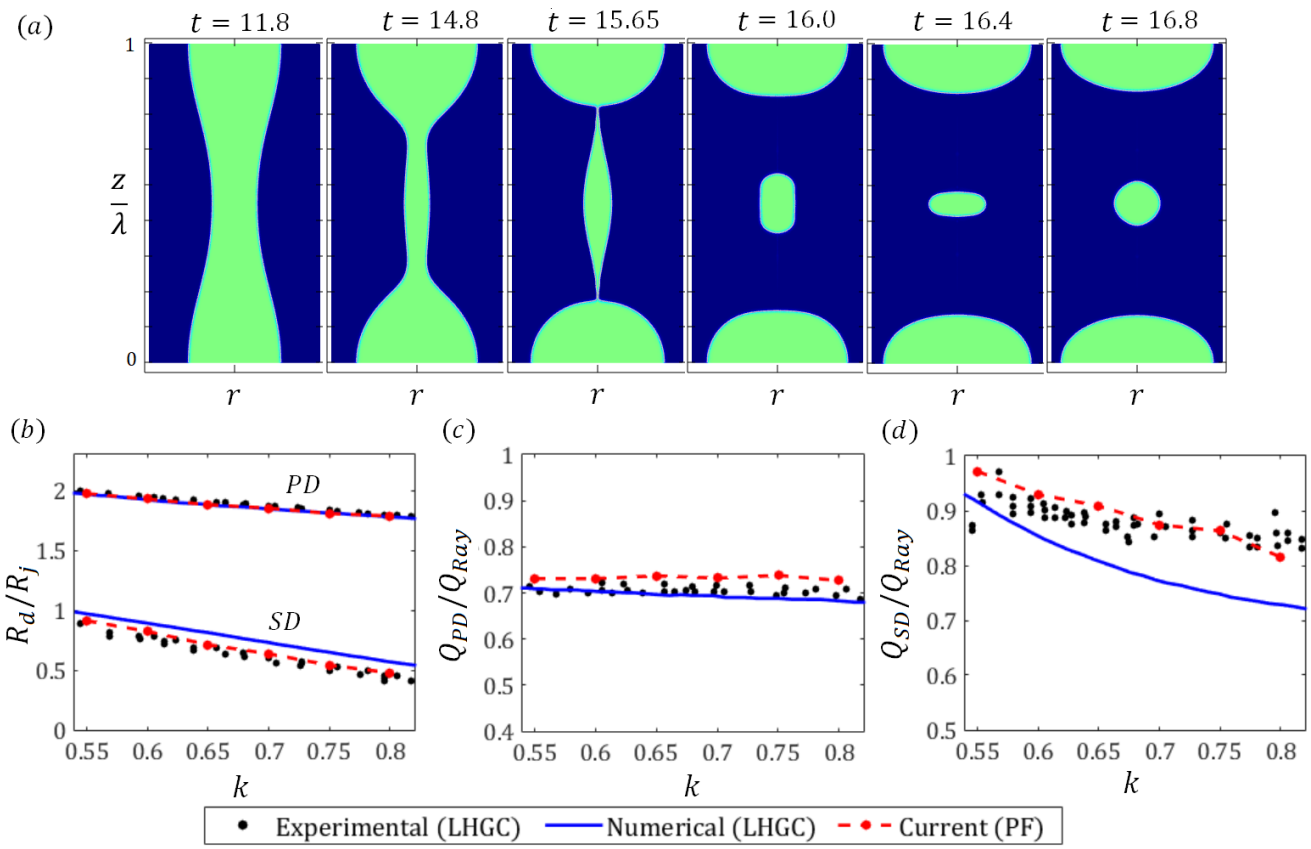

Figure 3.1: a) Evolution of the jet for $Oh = 0.079$, $\Gamma = 0.9$ and $k = 0.7$, the axial axis is normalized by λ; b) radii of primary and satellite droplets, comparison between the solution of the phase field model (PF) and the experimental and numerical data (LHGC) of López-Herrera and Gañán-Calvo [1] for $Oh = 0.079$, $\Gamma = 0.9$; c) charge of primary droplets; and d) charge of satellite droplets. Charges are normalized with the charge of the droplet at the Rayleigh limit.

to the slow viscous dissipation of its internal flow. Figure 3.1(b) compares the radii of the primary and satellite droplets. The radius R_d of a droplet is deduced from its volume right after pinch-off. The agreement between our calculations and the experiments and calculations of López-Herrera and Gañán-Calvo [1] is excellent. As the wavenumber increases the sizes of the primary and satellite droplets decrease monotonically, a trivial trend resulting from the volume of the jet yielding both droplets, $2\pi^2 R_j^2/k$, and the volume of the satellite being a small fraction of it. Figures 3.1(c) and 3.1(d) compare the charge of the primary and satellite droplets expressed as a fraction of the Rayleigh limit,

$$Q_{Ray} = 8\pi\sqrt{\varepsilon_o \gamma R_d^3}. \tag{3.1}$$

When the charge of a droplet is above the Rayleigh limit, the droplet becomes unstable and fragments into smaller droplets. The primary droplet is charged to a nearly constant fraction of the Rayleigh limit regardless of the wavenumber, while in the case of the satellite droplet this ratio increases modestly for decreasing wavenumber. Collins et al. [19] also found this trend in their equipotential study. Experimental images by López-Herrera and Gañán-Calvo [1] (see figure 9 in [1]) depicts how the primary droplet is much more radially elongated as the electrification level increases for the same viscosity level, a trend also observed in the numerical simulations. The thread connected to the primary droplet would subsequently undergo pinch-off forming the satellite droplet.

Figure 3.2 reproduces the analysis in Fig. 3.1 under more viscous conditions, $Oh = 0.271$, and equal electrification level, $\Gamma = 0.9$. Figure 3.2(a) shows that after the initial pinch-off separating the primary droplet and the satellite droplet, the retracting threads connected to the latter undergo a subsequent pinch-off that forms sub-satellite droplets. We observe this for all wavenumbers considered, $0.55 \leq k \leq 0.8$. Figure 3.2(b) compares the radii of PD and SD droplets. There is again excellent agreement between the phase field model and [1]. Moreover, the size of the SD droplets is slightly smaller than in the less viscous breakup.

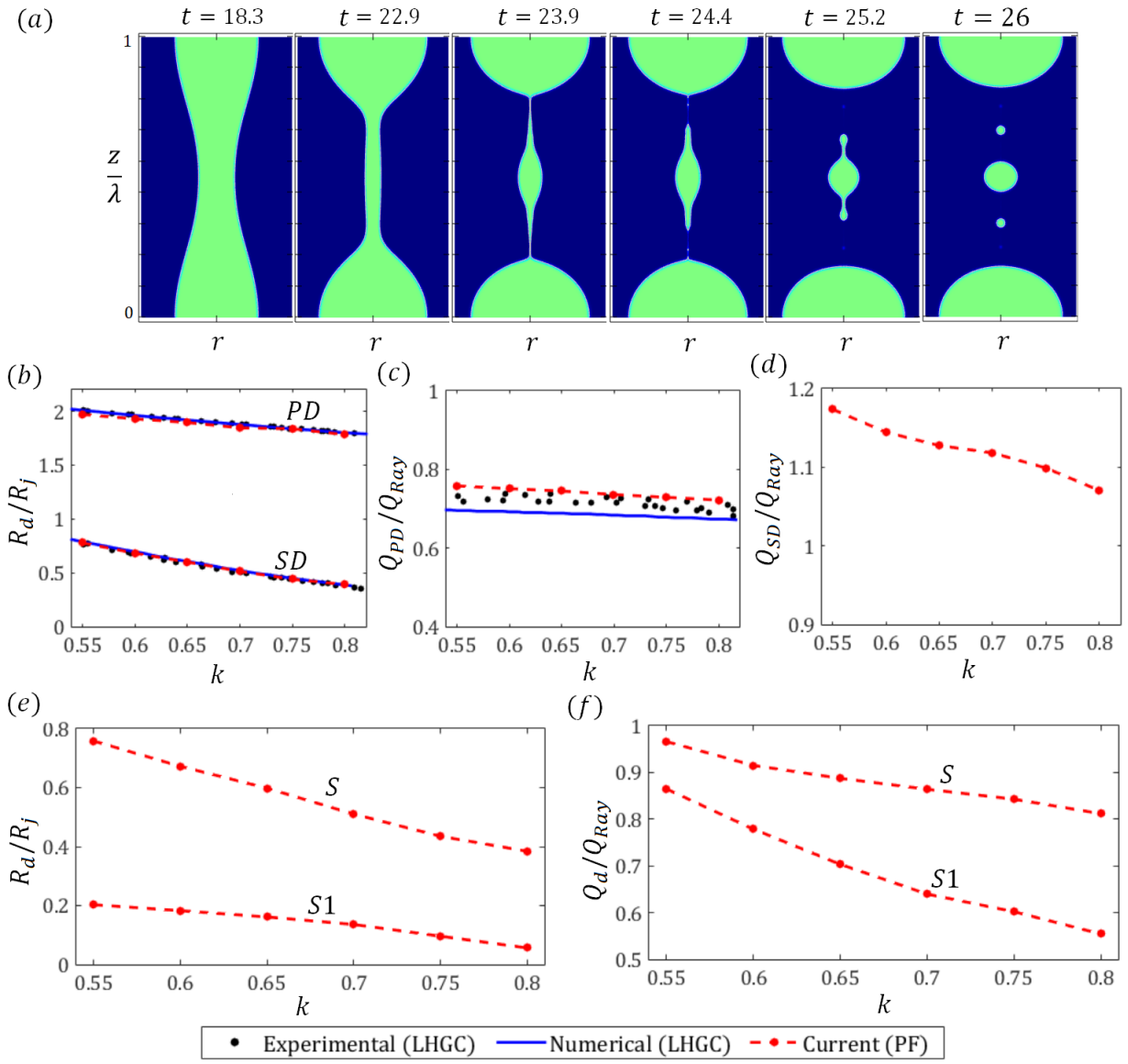

Figure 3.2: a) Evolution of the jet for $Oh = 0.271$, $\Gamma = 0.9$ and $k = 0.7$, the axial axis is normalized by λ; b) radii of primary and satellite droplets, comparison between the solution of the phase field model (PF) and the experimental and numerical data (LHGC) of López-Herrera and Gañán-Calvo [1] for $Oh = 0.271$, $\Gamma = 0.9$; c) charge of primary droplets (PD); d) charge of "Satellite Droplet" SD; (e) radius of the satellite (S) and sub-satellite (S1) droplets; and (f) charge of the satellite (S) and sub-satellite (S1) droplets. Charges are normalized with the charge of the droplet at the Rayleigh limit.

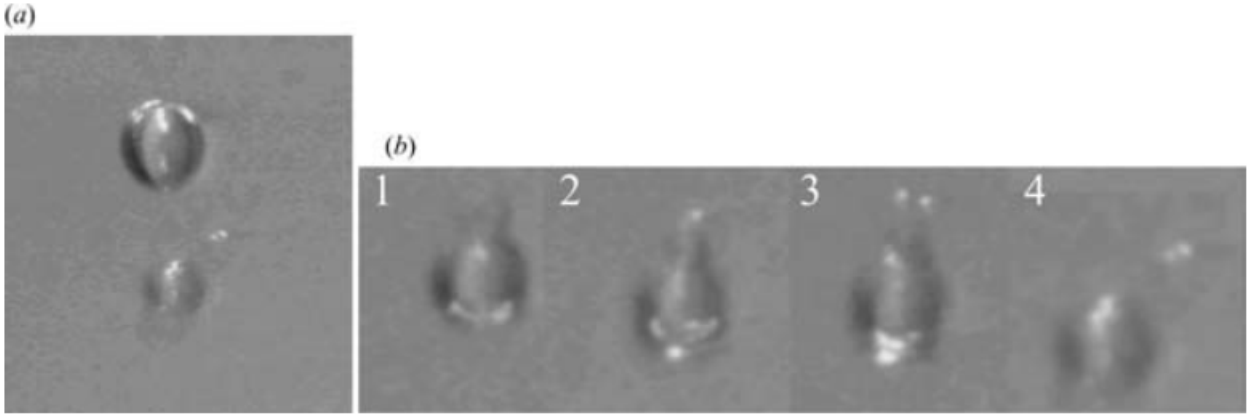

Figure 3.3: Experimental images obtained by López-Herrera and Gañán-Calvo [1] for $Oh = 0.271$ and $\Gamma = 0.9$ showing (a) The primary and satellite droplets; (b) 1-4 different stages of the breakup of satellite droplet "SD" (figure reproduced with permission, © 2004 Cambridge University Press)

Figure 3.2(c) shows that the primary droplets are charged below the Rayleigh limit, although at a slightly higher fraction than for $Oh = 0.079$; the SD droplets is now slightly smaller and takes less charge from the original jet section.

In their experimental study, López-Herrera and Gañán-Calvo [1] found that the SD droplets underwent subsequent breakups, however, they did not present the charge carried by them and simply argued that this subsequent breakup was a consequence of their charge levels exceeding the Rayleigh limit. Figure 3.3 depicts the experimentally obtained image where the authors claim that the satellite droplet undergoes subsequent fission as a result of "SD" being above the Rayleigh limit (see figure 3.3vb, snapshots 1-4 showing the disintegration of SD droplet). Numerically, figure 3.2(d) shows that the SD droplets are indeed charged above the Rayleigh limit. However, as evident from Fig. 3.2(a), this section of the jet resulting from the first pinch-off splits into additional droplets before it becomes spherical, with charges and diameters that can be quantified. Figure 3.2(e) depicts the radius of the satellite droplets S and $S1$ resulting from the second pinch-off, and Fig. 3.2(f) shows their charge levels. Interestingly, the second pinch-off reduces the charging level of both satellite droplets compared to the original SD droplet, so that the droplets actually forming

remain below the Rayleigh limit. This observation is also evident from the experimental image depicted in figure 3.3 (a) which shows that "SD" did disintegrate into "S" and "S1" droplets. However, we argue that the conclusion made in this prior experiment that "SD" did undergo Rayleigh fission is not accurate, as evident from the numerical simulations the retracting thread joining the Primary droplet (PD) with the Satellite droplet (SD) underwent natural instability to form subsatellite droplets which are below the Rayleigh limit.

In summary, previous studies [1, 19] have shown that the charge carried by the SD droplets increases with the Ohnesorge number (at constant Taylor number and wavenumber); the phase field model reproduces this too, and in addition shows that these SD droplets undergo additional pinch-offs during the jet breakup phase, yielding smaller droplets with charge levels (expressed as a fraction of the Rayleigh limit) smaller than that of the SD parent droplet. Chapter 4 will show that for higher electrification levels the satellite droplets S produced by the second pinch-off may exceed the Rayleigh limit.

Chapter 4

Role of Oh and Γ on Jet Breakup

4.1 Jet Breakup with Low Viscous Effect

We next study the breakup of jets with reduced viscous effects, $Oh = 0.1$, at varying levels of electrification and wavenumbers, $0 \leq \Gamma \leq 3$ and $0.5 \leq k \leq 1$.

Figure 4.1 depicts the evolution of the breakup at representative Taylor numbers and wavenumbers. For uncharged jets, Figure 4.1(a), the jet initially deforms with the radial velocity being negative at $z = \lambda/2$. This is because in the early stages of the deformation, $z = \lambda/2$ experiences the maximum capillary pressure. The pressure difference between $z = \lambda/2$ and $z = 0$ drives the early deformation of the jet pushing the fluid towards the ends of the jet section. As the deformation proceeds the radial velocity at $z = \lambda/2$ reverses its direction at $t = 17$ (k=0.5), leading to the formation of a satellite droplet [19, 27, 36]. Figure 4.1(b) depicts the deformation and breakup for an electrification level $\Gamma = 1$. In this case the reversal in the sign of the radial velocity of the interface at $z = \lambda/2$ occurs at an earlier stage due to the additional normal electric stresses acting on the interface, which leads to a greater bulge at $z = \lambda/2$. Subsequently, the jet breaks and forms satellite droplets larger

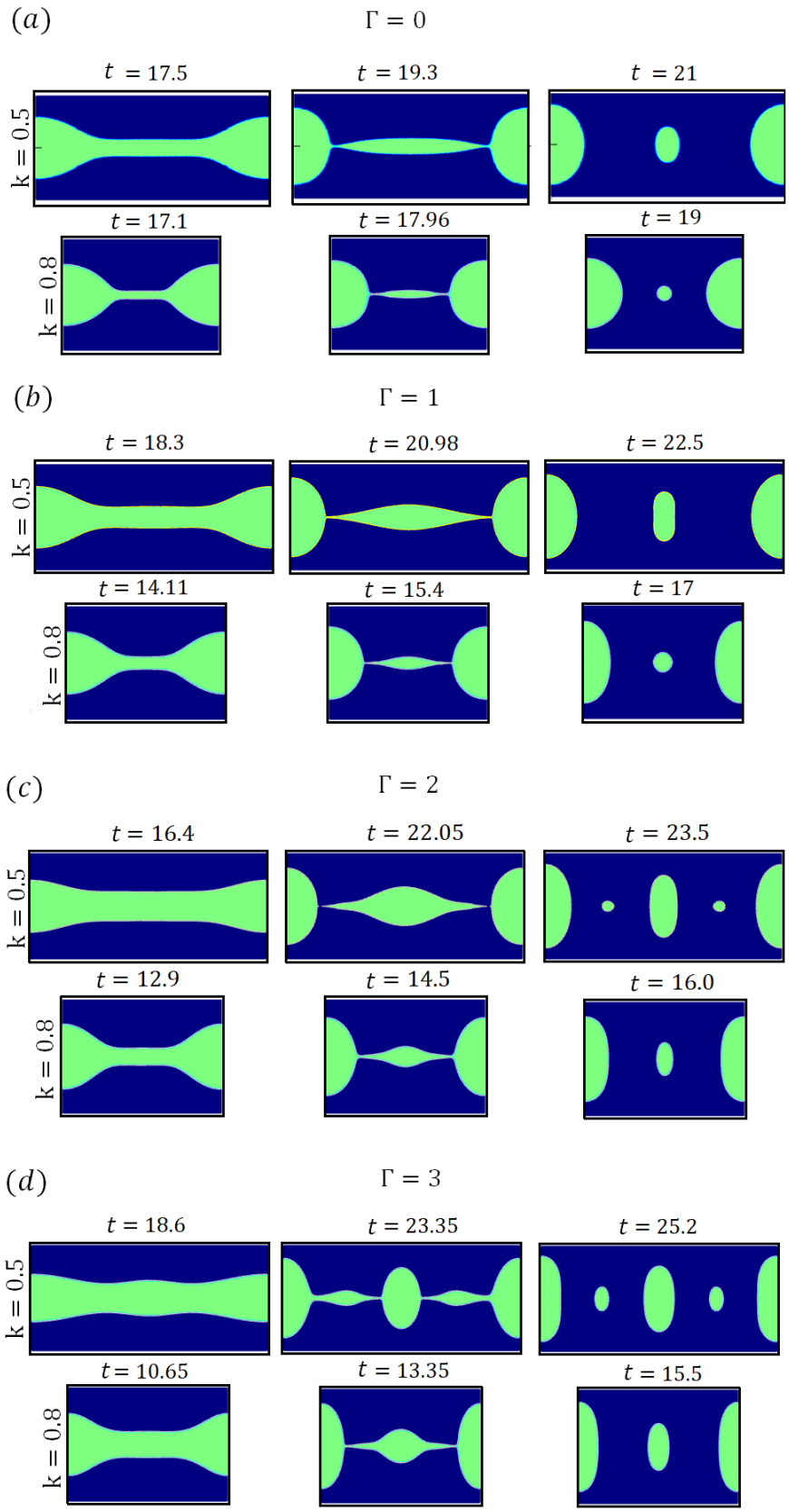

Figure 4.1: Evolution of breakups with small viscous effects, $Oh = 0.1$, for two wavenumbers $k = 0.5$ and $k = 0.8$, and several electrification levels: a) $\Gamma = 0$; b) $\Gamma = 1$; c) $\Gamma = 2$; and d) $\Gamma = 3$.

than in the uncharged breakup. It is worth noting that, for $\Gamma = 0$ and $\Gamma = 1$, only PD and SD droplets are formed for all the wavenumbers studied; i.e. we do not observe subsatellite droplets. Figures 4.1(c) and 4.1(d) depict the deformation and breakup of highly charged jets (it is worth restating that the electrostatic stress fully balances the capillary pressure in the nominal jet when $\Gamma = 2$). For $\Gamma = 2$ and $k = 0.5$, the retracting threads formed at the pinch-off undergo an additional breakup leading to the formation of sub-satellite droplets. For $\Gamma = 3$ and $k = 0.5$ the radial velocity reversal at $z = \lambda/2$ occurs at a much earlier stage due to the larger electrostatic stresses. The breakup differs in this case in that the first pinch-off actually happens in the thread attached to the S droplet, rather than near the PD droplet. Subsequently and as depicted in the first row in Figure 4.1(d), the retracting thread joined to the primary droplet undergoes a second pinch-off leading to the formation of an $S1$ droplet. Therefore, highly charged jets with long wavelengths lead to the formation of sub-satellite droplets even at low viscosities.

Figure 4.2(a) depicts the time at the first pinch-off, which can be regarded as the breakup time. For $0.6 < k < 1$, the breakup time decreases at increasing Taylor number, a trend also observed by Collins et al. [19] and Lakdawala et al. [27]. Moreover, the wavenumber with minimum breakup time increases with the Taylor number, i.e. the modal droplet becomes smaller at increasing electrification level. Figures 4.2(b) and 4.2(c) show the radius of the primary and satellite droplets. At fixed wavenumber the radius of the primary droplet decreases at increasing Taylor number because of the earlier reversal in the radial velocity of the interface, which increases the size of the satellite droplet. Sub-satellite droplets are not formed at either $\Gamma = 0$ or $\Gamma = 1$, and start to appear at $\Gamma = 2$ and sufficiently long wavelengths. Figure 4.2(d) depicts the charge carried by the primary droplet as a fraction of the Rayleigh limit. As already observed in Figures 3.1 and 3.2, this ratio is relatively independent of the wavenumber, and increases with the Taylor number. Primary droplets exceed the Rayleigh limit for $\Gamma \gtrsim 1.5$, an important result for predicting the stability of primary droplets in low viscous breakups. Figure 4.2(e) shows the charges carried by the

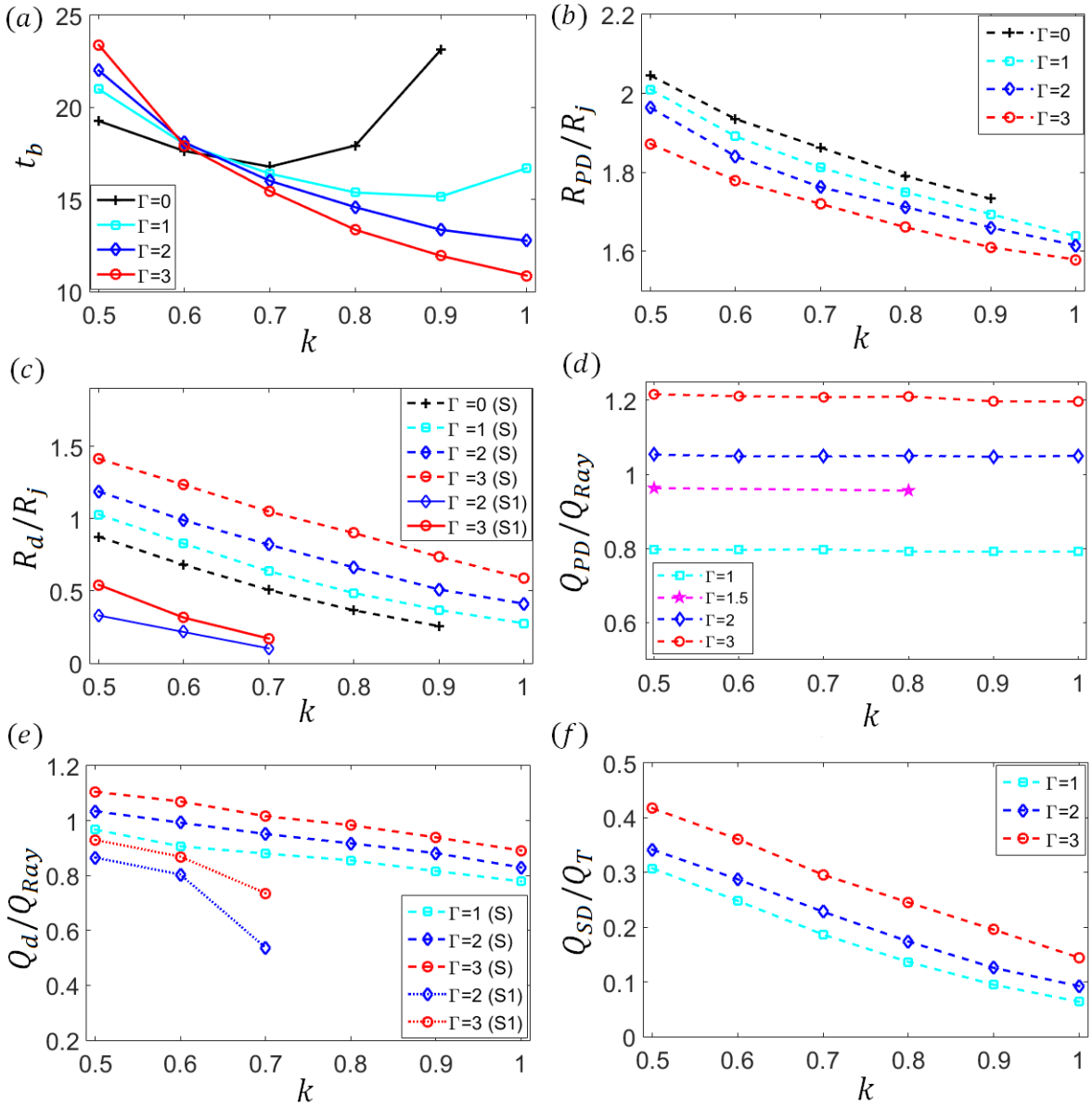

Figure 4.2: Results of the phase field model for breakups with small viscous effects, $Oh = 0.1$, as a function of the Taylor number and wavenumber: a) time at first pinch-off; b) radius of primary droplets; c) radius of S and $S1$ satellite droplets; d) charge of the primary droplet relative to its Rayleigh limit; (e) charge of the S and $S1$ satellite droplets relative to their Rayleigh limit; (f) fraction of the total charge carried by the satellite droplets.

satellite droplets. Although subsatellite droplets are being formed, the S droplets are above the Rayleigh limit for $\Gamma \geq 2$ and the longer wavelengths. On the other hand the $S1$ droplets are always charged below the Rayleigh limit. Finally, Figure 4.2(f) shows the fraction of the total charge carried by the satellite droplets.

Figure 4.3(a) shows the electric potential, with arrows representing the direction and strength of the electric field, when the radial velocity of the interface at $z = \lambda/2$ becomes zero before reversing its direction, together with profiles of the radial velocity, axial velocity, potential and normal component of the electric field along the surface. The radial velocity at this time displays minima at $z = 0.35\lambda$ and $z = 0.65\lambda$, which starts creating the curvature for the satellite droplet that will eventually form. The electric potential along the surface is nearly constant, i.e. the jet can be regarded equipotential to a good approximation, as should be expected from the small value of Π_ℓ; furthermore, the potential has very slightly dropped from its initial value of 1 at this point. The electric field on the surface at $z = 0.25\lambda$ and $z = 0.75\lambda$ is partially shielded by the inward bending of the surface, and hence its normal component displays local minima at these points, while there are local maxima at $z = 0$, $\lambda/2$ and λ. Figure 4.3(b) depicts the same variables immediately before the first pinch-off. The electric potential along the surface is slightly lower near the pinch-off, a feature also observed by López-Herrera and Gañán-Calvo [1], because the capillary time associated with the local radius of the surface becomes comparable to the electric relaxation time. The radial velocity displays two distinct minima, which later separate the primary and sub-satellite $S1$ droplets from the satellite S droplet. Figure 4.3(c) includes three snapshots with mappings of the electric potential after the first pinch-off, including the formation of a sub-satellite droplet. The maximum values of the normalized electric field on the S and $S1$ droplets are 1.98 and 2.37 respectively, and occur at the farthest point from the axis. In particular, the $S1$ droplet features the maximum value of the electric field at any point and time of the calculation.

Figure 4.4 depicts the evolution of the breakup leading to the formation of a sub-satellite

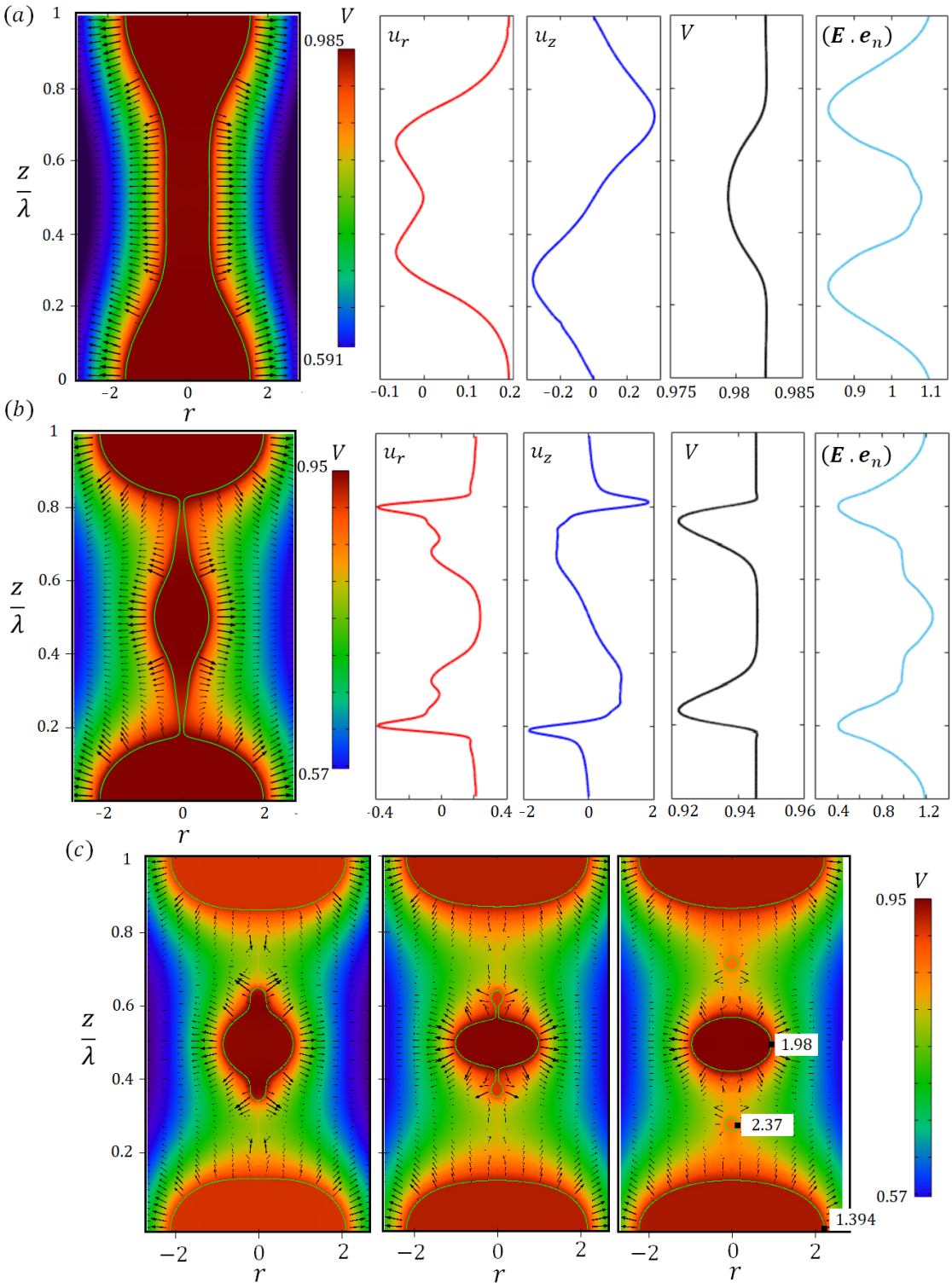

Figure 4.3: Electric potential map and radial velocity, axial velocity, potential and normal component of the electric field on the surface, for $Oh = 0.1$, $\Gamma = 2$ and $k = 0.7$: a) solution at $t = 13.7$ coinciding with zero radial velocity at $z = \lambda/2$; b) solution just before pinch-off. c) Electric potential maps before ($t = 16.6$), near ($t = 16.95$), and after ($t = 17.9$) the second pinch-off. The last inset shows the maxima of the electric field.

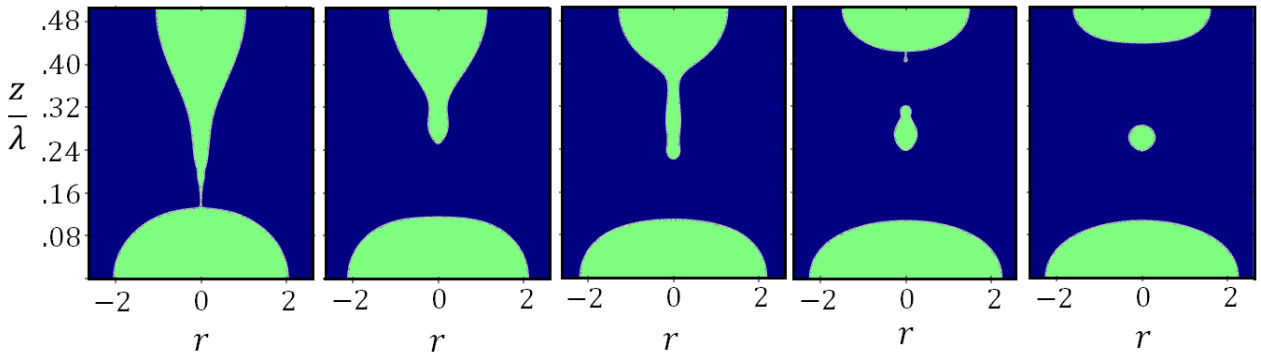

Figure 4.4: Retracting thread and sub-satellite formation process for $k = 0.5$, $\Gamma = 2$ and $Oh = 0.1$

droplet ($k = 0.5$, $\Gamma = 2$, $Oh = 0.1$). A tapered thread connecting the primary droplet and the soon-to-be satellite droplet is severed by the first pinch-off, and retracts towards the SD droplet due to the higher pressure in the tapered end. However, the thread does not fully collapse into the bulk of the liquid, but it starts to elongate backwards toward the primary droplet (see third inset). This thread eventually undergoes a second pinch-off, leading to the formation of the S and $S1$ droplets.

4.2 Jet Breakup with High Viscous Effect

Figures 4.5-4.8 reproduce the same simulations as in Section 4.1, but for a large Ohnesorge number exemplifying dominant viscous effects, $Oh = 10$. The geometry of the deforming jet displays several differences with respect to the $Oh = 0.1$ case. In the absence of electrification, Figure 4.5(a), no satellite or sub-satellite droplets form. Since inertial effects are negligible, the pressure remains maximum at $z = \lambda/2$ until pinch-off, preventing the formation of satellite droplets [19, 49]. Figure 4.5(b) shows the evolution for a Taylor number of one. In this case satellite and sub-satellite droplets form, not driven by inertia but by the electrostatic pressure in the vicinity of $z = \lambda/2$. At the larger Taylor numbers shown in Figures 4.5(c) and 4.5(d), $\Gamma = 2$ and $\Gamma = 3$, three distinct sub-satellite droplets are formed

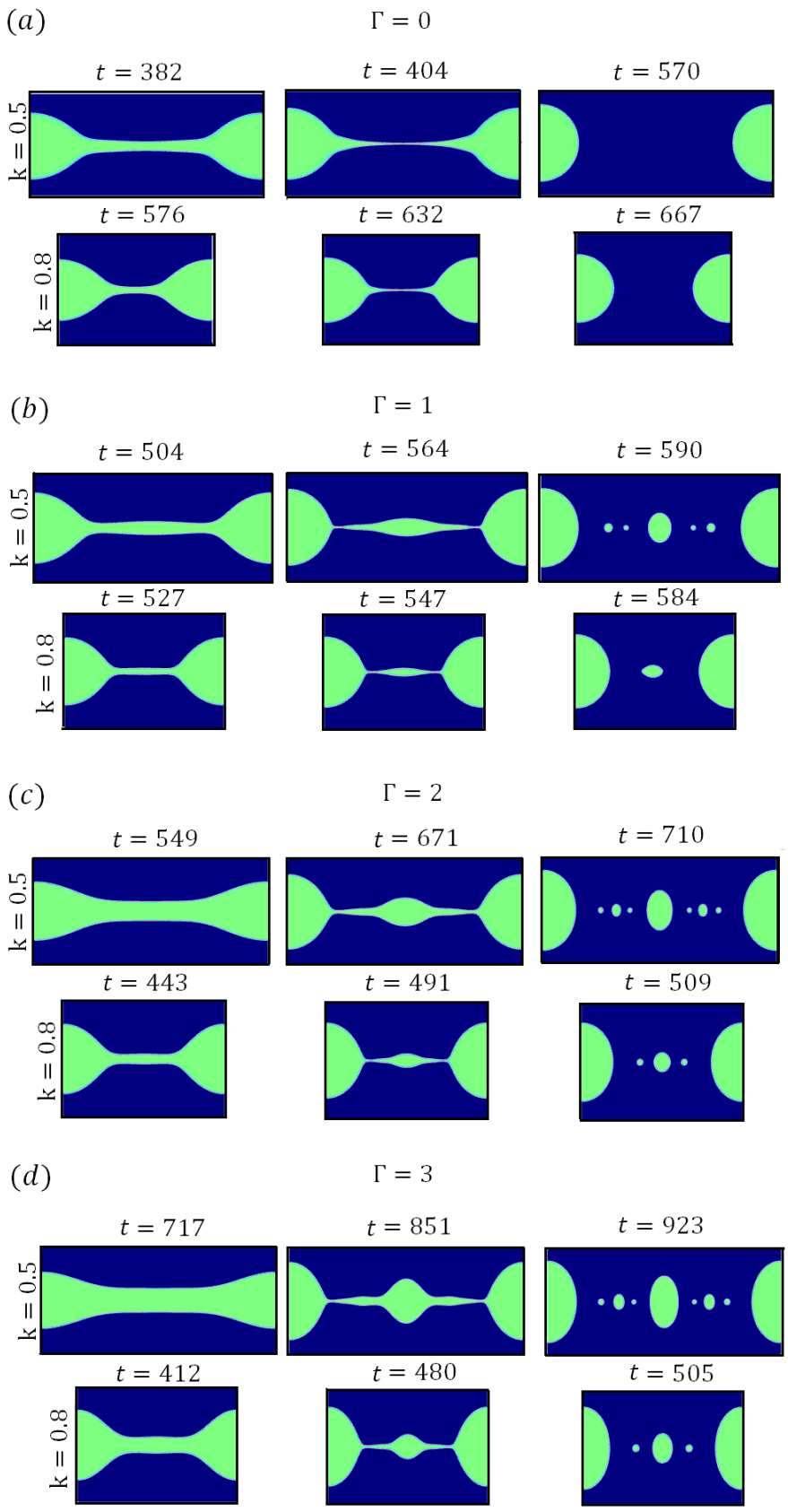

Figure 4.5: Evolution of breakups with high viscous effects, $Oh = 10$, for two wavenumbers $k = 0.5$ and $k = 0.8$, and several electrification levels: a) $\Gamma = 0$; b) $\Gamma = 1$; c) $\Gamma = 2$; and d) $\Gamma = 3$.

along with the primary and satellite droplets for $k = 0.5$, and single sub-satellite droplets are formed for the shorter jet section, $k = 0.8$. The mechanism for the formation of the initial SD droplet is different when compared to the $Oh = 0.1$ case. At small Ohnesorge number the SD droplet is connected to the primary droplets by a tapered thread, whereas at large Ohnesorge number the thread joining the primary and SD droplets is slender and thin. The slender thread coupled with the lack of inertial effects leads to the formation of multiple sub-satellite droplets. The breakup behavior is qualitatively similar to that observed in prior studies of highly viscous and uncharged jets (Stoke's limit) surrounded by a fluid of comparable viscosity [21, 22, 29, 30].

The times of the first pinch-off, Figure 4.6(a), are over one order of magnitude larger than in Fig. 4.2(a). t_μ rather than t_c is the appropriate characteristic time for describing the dynamics because inertial effects are negligible, but since we continue using t_c to normalize time the breakup times are much larger than one. Note also that for a given Taylor number, the wavenumber with minimum breakup time decreases at increasing Onhesorge number. Thus, the wavelength that produces the modal primary droplet increases with the importance of viscous effects, while the intensity of electrification has the opposite effect. The radius of the primary droplets, Figure 4.6(b), displays a similar trend as in the low viscosity regime, i.e. the size of the primary droplet decreases as the level of electrification increases due to the larger electric stresses on the interface which leads to the formation of larger satellite droplets. Figure 4.6(c) depicts the radii of the S and $S1$ droplets (no satellite droplets are formed for $\Gamma = 0$). We only display the radius of $S1$ sub-satellite droplet, although two additional sub-satellites are formed for $k = 0.5$; for all the other wavenumbers only the $S1$ sub-satellite droplet forms. The size of the S droplets for a given Γ is smaller in the high viscous regime than in the low viscous regime. This trend could be explained by the fact that in the low viscous case, along with the electric stresses, inertial effects also help in pushing the fluid to the satellite droplet, hence increasing its size. This additional inertial mechanism is not present at $Oh \gg 1$. The trends for the charge of the different droplets relative to the

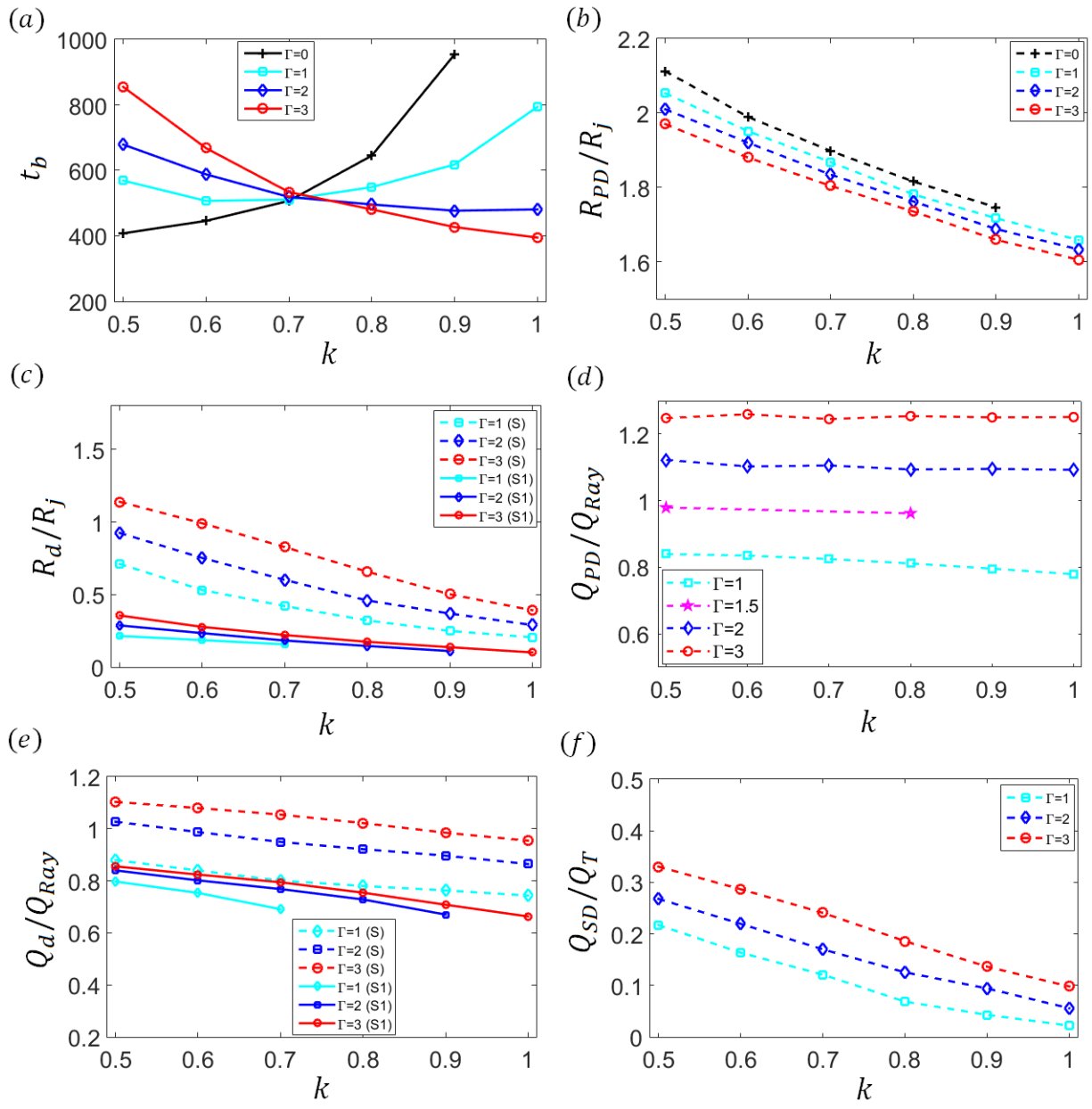

Figure 4.6: Results of the phase field model for breakups with high viscous effects, $Oh = 10$, as a function of the Taylor number and wavenumber: a) time at first pinch-off; b) radius of primary droplets; c) radius of S and $S1$ satellite droplets; d) charge of the primary droplet relative to its Rayleigh limit; (e) charge of the S and $S1$ satellite droplets relative to their Rayleigh limit; (f) fraction of the total charge carried by the satellite droplets.

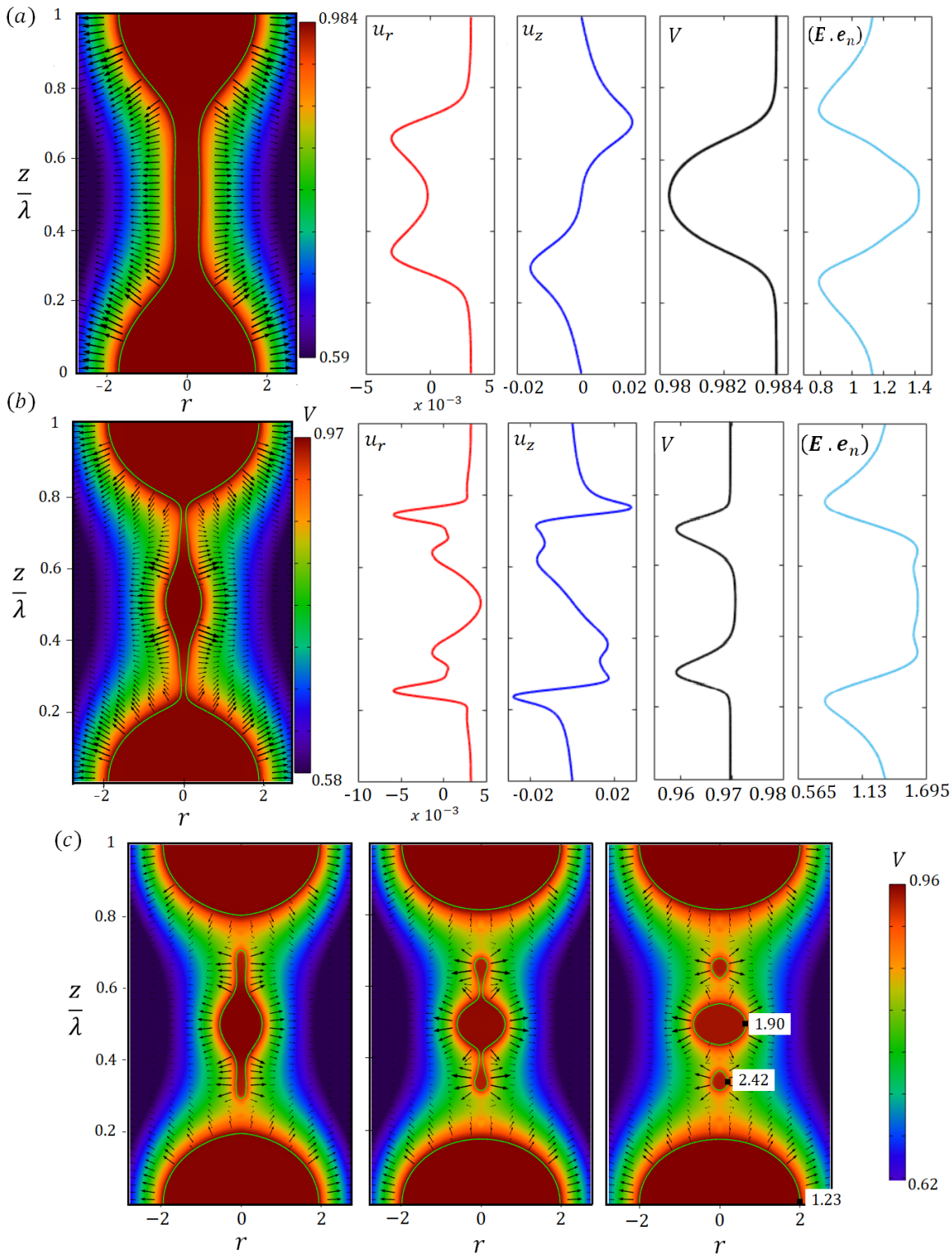

Figure 4.7: Electric potential map and radial velocity, axial velocity, potential and normal component of the electric field on the surface, for $Oh = 10$, $\Gamma = 2$ and $k = 0.7$: a) solution at $t = 453$ coinciding with zero radial velocity at $z = \lambda/2$; and b) solution just before pinch-off. c) Electric potential maps before ($t = 538$), at ($t = 554$), and after ($t = 568$) second pinch-off. The last inset shows the location and values of electric field maxima.

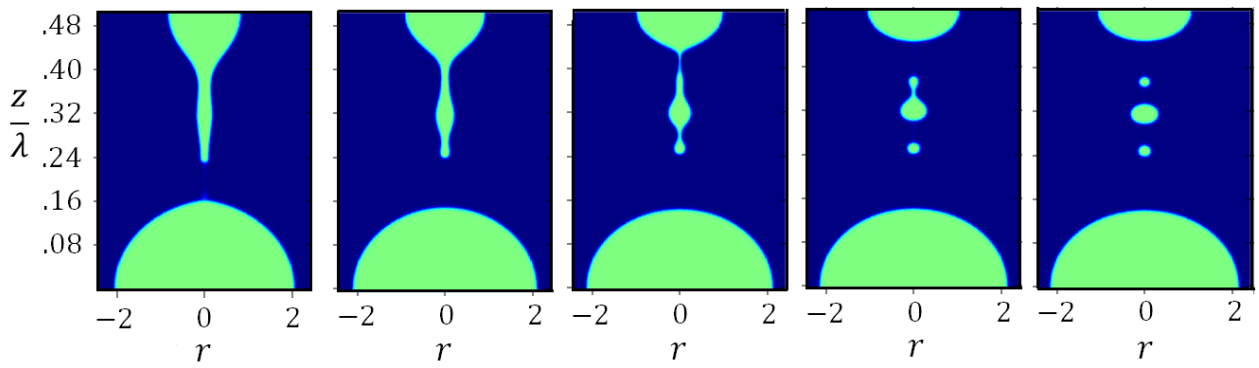

Figure 4.8: Formation of sub-satellite droplet from the retracting slender thread for $Oh = 10$, $\Gamma = 2$ and $k = 0.5$. $z/\lambda = 0$ depicts the primary droplet location and $z/\lambda = 0.5$ depicts the location of the satellite droplet.

Rayleigh limit, Figures 4.6(d) and 4.6(e), are similar to the low viscosity case. Again, in Figure 4.6(d) we include results for $\Gamma = 1.5$ indicating that this value of the Taylor number separates primary droplets that are above ($\Gamma \gtrsim 1.5$) and below ($\Gamma \lesssim 1.5$) the Rayleigh limit, i.e. droplets that are unstable and stable. Interestingly, this stability condition for the primary droplets is largely independent of the wavenumber and the Onhesorge number. Finally, note that the fraction of the total charge that is carried by satellite droplets is reduced in a breakup dominated by viscous effects (compare Figures 4.6(f) and 4.2(f)).

The surface profiles and electric potential maps in Figure 4.7 display similar trends to the $Oh = 0.1$ case. At any given time, the surface is equipotential to a good approximation. In fact, our definition of Π_t overestimates the time constant for charge relaxation, because t_μ is the correct characteristic time for the evolution of the jet at high Ohnesorge number, and $t_\mu \gg t_c$. The electric field is normal to the surface of the jet, and displays local maxima at the centers of the primary and subsatellite droplets with an absolute maximum on the smallest subsatellite. In Figure 4.7(b) for a time close to the first pinch-off we note a distinct feature connected to the formation of subsatellite droplets: in addition to the typical local minima of the radial velocity at $z = 0.2\lambda$ and $z = 0.8\lambda$ leading to the location of the first pinch-off, two additional local minima appear at $z = 0.4\lambda$ and $z = 0.6\lambda$ which lead to the thinning of the retracting thread and eventually to a second pinch-off and sub-satellite droplets. Similar

features are also observed in the axial velocity profile.

Figure 4.8 depicts the breakup behavior of the retracting thread for $\Gamma = 2$ and $k = 0.5$. Although the retracting thread moves towards the satellite droplet, the thread is detached from the satellite droplet by a second pinch-off and subsequently undergoes additional pinch-offs to form subsatellite droplets. When compared with the breakup in Figure 4.7(c) for the same Taylor number and smaller wavenumber, $k = 0.7$, the behavior is similar but the longer thread produced by the smaller wavenumber leads to a larger number of subsatellite droplets.

4.3 Droplet Stability Criteria

For a perfectly conducting inviscid cylinder, the critical Rayleigh stability limit is given by $\Gamma_{Ray} = 1.5$ [20]. We make additional simulation runs for the low viscosity ($Oh = 0.1$) and high viscosity ($Oh = 10$) regime for $\Gamma = 1.5$ (only for wavenumbers of 0.5 and 0.8).

Figure 4.9 depicts the charge of the primary (PD) and satellite (S) droplets for different wavenumbers and viscosity regime discussed in the current article. As evident from figure 4.9, for $\Gamma \leq 1.5$, the droplets formed after the breakup of the jet are always below the Rayleigh charge limit, with the droplets formed for $\Gamma = 1.5$ being very close to the Rayleigh charge limit (approximately 3-4 percent below the Rayleigh charge limit). It must be noted that, while figure 4.9 only depicts the charge carried by primary and satellite droplets, the sub-satellite droplets are also below the Rayleigh charge limit. As shown in Chapter 2 and in prior numerical studies [1, 17, 19], for high viscosity cases the SD droplets could exceed the Rayleigh limit for $\Gamma \leq 1.5$; however, the number of sub-satellite droplets also increases with the increase in viscosity levels, bringing the total charge carried by the satellite (and sub-satellite) droplets below the Rayleigh limit for all the viscosity regimes.

Consequently, we may conclude that for $\Gamma \leq 1.5$, the wide distribution in the size of droplets

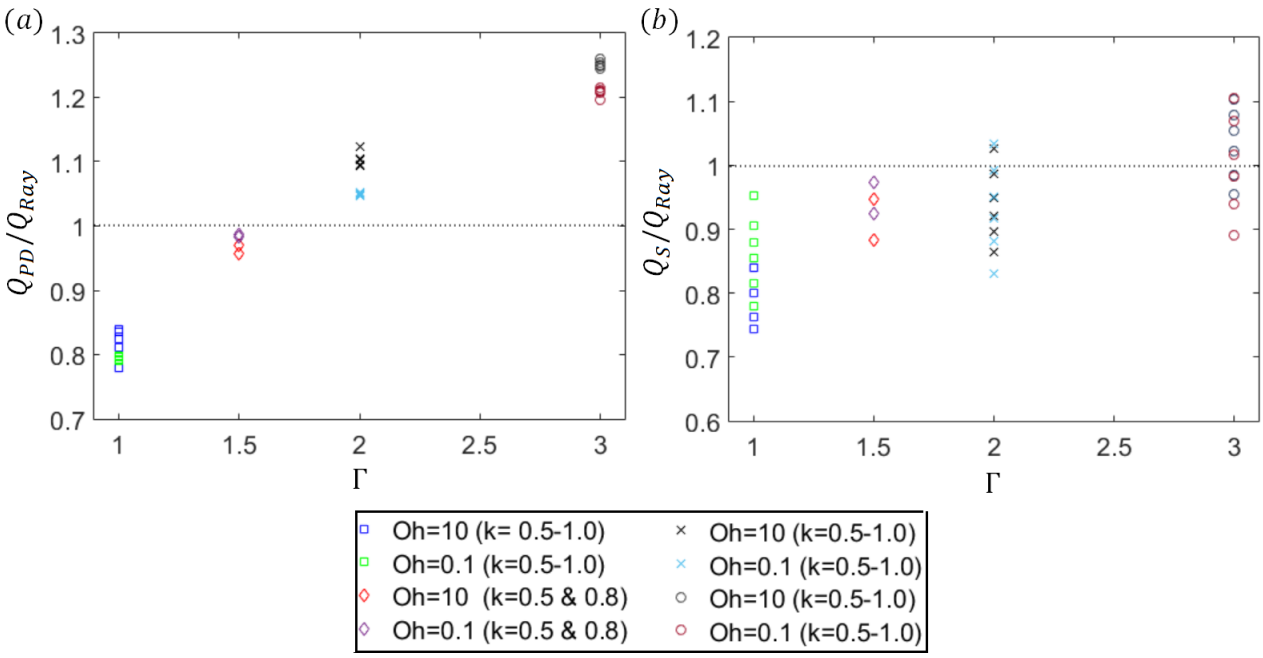

Figure 4.9: (a) Charge of the primary droplet (PD) and; (b) charge of satellite droplet (S) with respect to Rayleigh charge limit for different k, Oh and Γ values.

in the high viscosity regime favors the stability of the droplets. All these trends, however are only valid below the critical Taylor number Γ_{Ray}. Recent experimental results by Yang et al. [50] confirms the predictions made by the phase-field model, as evident from figure 4 (a) and (b) of Yang et al. [50] for $\Gamma = 0.99$ the primary and satellite droplets appear to be stable and do not unndergo any further fission. However for $\Gamma = 1.63$, the droplets are evidently unstable and undergo subsequent fission.

4.4 Jets with maximum growth rates

As discussed in Chapter 2, the mode of the diameter distribution of primary droplets can be estimated with a linear stability analysis of the breakup, which yields the wavenumber of maximum growth rate, also known as the critical wavenumber k^*, as a function of Γ and Oh. The jet section associated with the critical wavenumber is expected to evolve into the modal primary droplet. Figure 4.10 shows $k^*(\Gamma, Oh)$ for two Ohnesorge numbers, 10 and

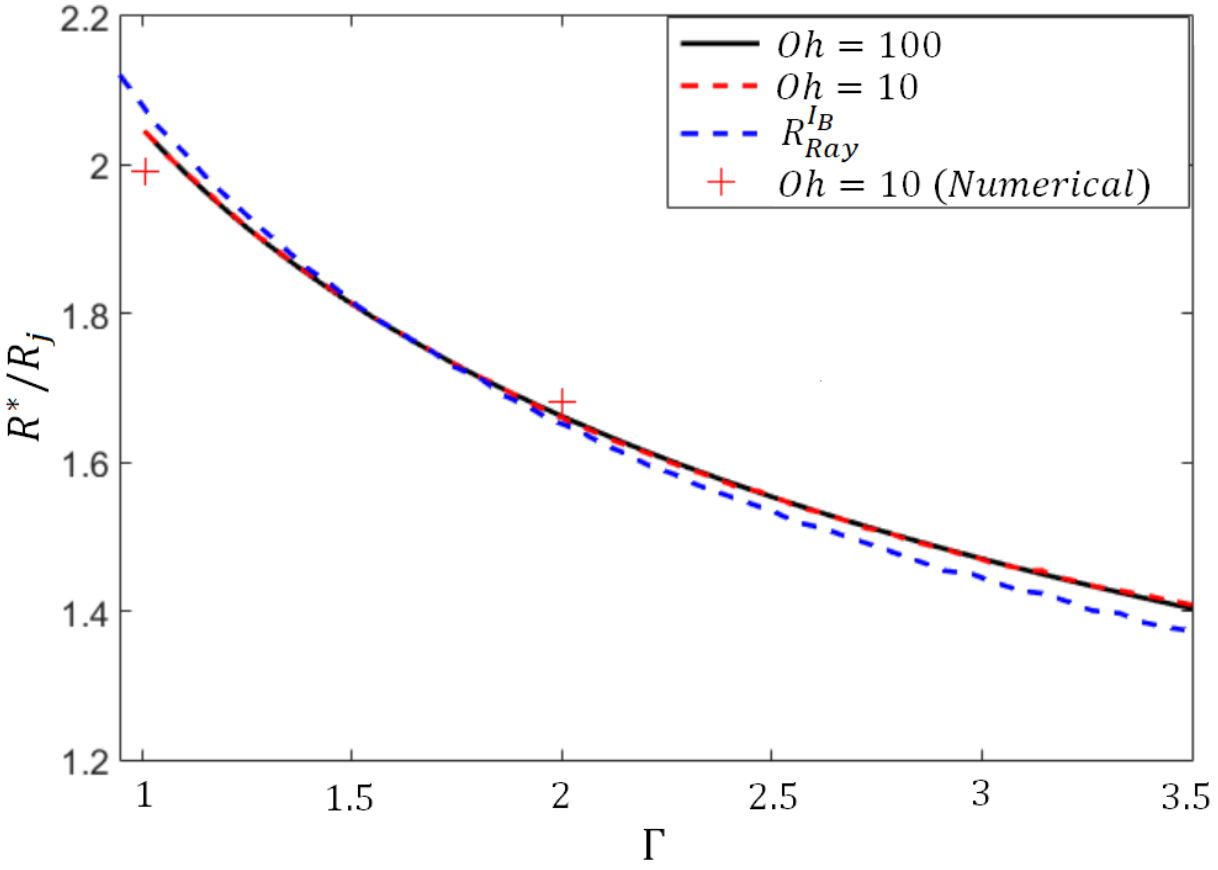

Figure 4.10: Droplet radius (predicted from the associated critical wavenumber (k^*) as a function of the Taylor number obtained with linear stability theory. Comparison with two wavenumbers of fastest pinch-off (phase field model), and the radius $R^{I_B}_{Ray}$ of the droplet charged at the Rayleigh limit and having the jet's charge-to-mass ratio.

100, as well as the associated droplet diameter [31]. For the large values of the Ohnesorge and Taylor numbers, the critical wavenumber does not depend on the Ohnesorge number and is only a function of the Taylor number. Figure 4.10 also plots the radius of the droplet that, having the charge-to-mass ratio of the undisturbed jet, is charged at the Rayleigh limit [31]:

$$\frac{R^{I_B}_{Ray}}{R_j} = (9/\Gamma)^{1/3}. \tag{4.1}$$

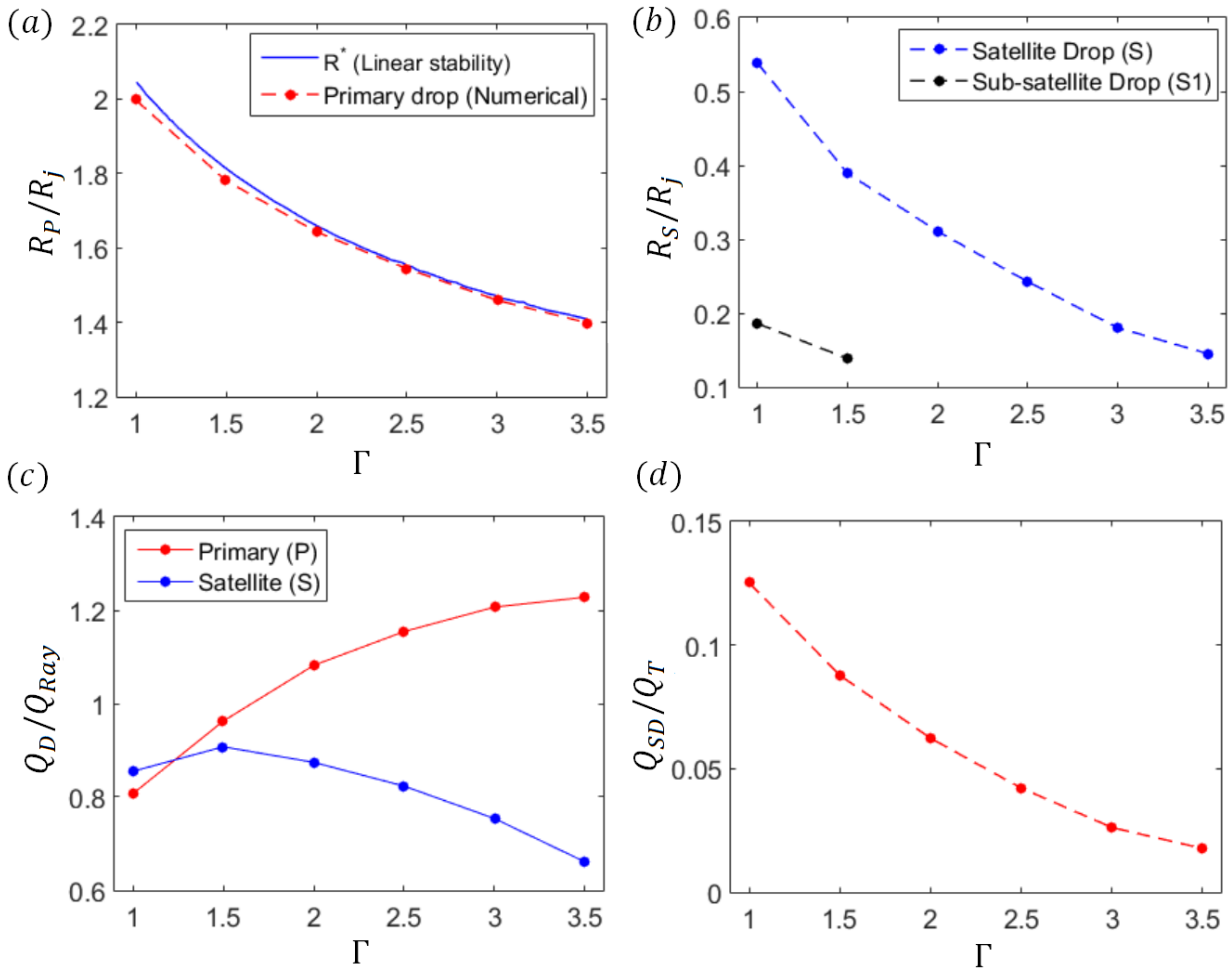

Figure 4.11: Phase field model prediction for wavenumbers associated with maximum growth-rate for different Taylor numbers- (a) normalized radius of the primary droplet along with the modal radius suggested by linear stability analysis, (b) normalized radius of satellite (S) and sub-satellite droplet (S1), (c) dimensionless charge carried by primary and satellite droplet, (d) fraction of total charge carried by the satellite droplet.

This curve indicates that, in the absence of satellite droplet formation, the modal droplet would be above the Rayleigh limit for $\Gamma \geq 1.54$, a trend also observed from the non-linear breakup model and previous studies [50]. Figure 4.10 also includes the radius of the primary droplets with the fastest pinch-off time for $\Gamma = 1$ and $Oh = 10$, and for $\Gamma = 2$ and $Oh = 10$, interpolated from Figure 4.6(a). These two points are near the $k^*(\Gamma, Oh)$ curve, supporting the use of linear stability analysis to estimate the modal wavenumber in the natural breakup.

Figure 4.11 summarizes the solution of the non-linear breakup model for droplets in the

Stokes limit $Oh = 50$. The radii of the main droplets predicted by the non-linear model, Figure 4.11(a), is smaller than the critical radius obtained with linear stability analysis because of the formation of satellite droplets at all flow rates (low Taylor numbers, corresponding to smaller critical wavenumber), Figure 4.11(b). The difference with the critical radius is small because the volume of the satellite droplet is a small fraction of the volume of the jet section; this fraction becomes smaller as the critical wavenumber, or equivalently the Taylor number, increase. The breakup produces satellites droplets at all beam currents, and sub-satellite droplets only near the minimum flow rate ($\Gamma_{min} = 1.2$). Since the formation of sub-satellites is enhanced by increasing electrification and decreasing wavenumber, their absence for $\Gamma > 1.5$ suggests that the decreasing value of the critical wavenumber at increasing Taylor number is preventing the otherwise expected proliferation of sub-satellite droplets. Figure 4.11(c) shows that the primary droplets are charged above the Rayleigh limit for $\Gamma \gtrsim 1.5$, while the satellite droplets are always below the Rayleigh limit, with the maximum charge level achieved at close to $\Gamma = 1.5$. Since at fixed Taylor and Ohnesorge numbers all primary droplets are approximately charged at the same fraction of the Rayleigh limit regardless of the wavenumber, most primary droplets of electrosprays operating at flow rates such that $\Gamma > 1.5$ will be charged above the Rayleigh limit (see equation 2.42 which relates flow rate $\Pi_Q \sim \Gamma^2$). Therefore, we expect the fragmentation of primary droplets caused by Coulomb explosions to be common in electrosprays with relatively high flow rates. Figure 4.11(d) depicts the fraction of total charge carried by the satellite droplets. It is evident that for highly charge jets, the primary droplets would be carrying majority of the total charge primarily because of the large critical wavenumbers associated with the high electrification levels, therefore, leading to much smaller satellite droplets (if any). It is worth noting that, since this study deals with high electrification level, it is possible that, for large Γ, the jet undergoes whipping instability (i.e. the jet breakup won't be axi-symmetric anymore), therefore the model can potentially fail for extreme electrification levels.

Chapter 5

Conclusions and Future Work

5.1 Conclusions

We have developed a leaky-dielectric phase field model to study the deformation and breakup of electrified jets of finite conductivity, performing calculations in wide ranges of the Taylor number, the Ohnesorge number and the wavenumber. The phase-field method allows us to accurately model the deformation of the jet beyond the first pinch-off, and therefore makes it possible to study the formation of sub-satellite droplets. However, one of the caveats of the phase field model or perhaps any level set method is the use of finite thickness of the artificial diffuse interface. There could be an inherent possibility (specifically for highly viscous regime) that there exists significantly smaller sub-satellite droplets whose size is smaller than the diffuse interface thickness ξ which cannot be resolved by the numerical model. However, since in our calculations $\xi = 1/66$, this potential loss in information for significantly smaller sub-satellite droplets is not detrimental. We draw the following main conclusions:

1. There is an excellent agreement between the solution of the phase field model and

the experimental and numerical results of López-Herrera and Gañán-Calvo [1]. The radius of the satellite droplet increases at decreasing Ohnesorge number for fixed Taylor number and wavenumber. For high Ohnesorge number, the satellite droplet SD would be above the Rayleigh limit even at relatively low values of the Taylor number, but it does not form because the retracting liquid threads tend to undergo additional pinch-offs that distribute the charge into sub-satellite droplets at charge level below the Rayleigh limit. This phenomenon can only be observed with a phase-field model like the one developed in this article.

2. The Ohnesorge number plays a key role in the size distribution of the droplets. In a highly viscous breakup, the satellite droplet is connected to the primary droplet by a long and slender thread, which undergoes additional pinch-offs to create sub-satellite droplets. This feature also exists at low Ohnesorge number and high Taylor number. However, due to the shape of the retracting thread and inertia, fewer sub-satellite droplets are produced.

3. The Taylor number also plays a key role in the size distribution of the droplets. Irrespective of the importance of viscous effects, an increasing level of electrification increases the size of the satellite droplet and hence reduces the radius of the primary droplet. Moreover, the formation of sub-satellite droplets is enhanced by increasing electrification levels.

4. We show that the value 1.5 for the Taylor number separates primary droplets that are above the Rayleigh limit and would be unstable ($\Gamma \gtrsim 1.5$), from primary droplets that are below the Rayleigh limit ($\Gamma \lesssim 1.5$), regardless of the wavenumber and the Ohnesorge number.

5. We present formulae for relating the dimensionless numbers parametrizing the phase field model (Γ, Oh and Π_t) with those parametrizing the state of a cone-jet (Π_Q and Re_K), in order to apply it to the natural breakup of cone-jets.

5.2 Future Work

There are many areas which still need clarity and further investigation. Two evident directions worth exploring are:

First, from the numerical calculations it is clear that the charged primary droplets are above the Rayleigh limit for $\Gamma_R > 1.5$. Therefore, these primary droplets are expected to undergo fission, where they break into smaller charged droplets. This mechanism allows the primary droplet to shed a large fraction of charge thereby, bringing them below the Rayleigh limit. The final size distribution of the progeny droplets formed after the Rayleigh fission and charging level of the parent and progeny droplets is unknown for these primary droplets. Current model could not account for this fission mechanism.

Secondly, for highly charged jet (large Γ) the jet undergoes whipping instability, where the electrostatic forces acting on the jet surface are strong enough to induce lateral instability. The current model is only limited to axisymmetric breakup of electrified jets; therefore, the whipping instability cannot be predicted with the current model. Whipping instability is the primarily more evident for electrosprays operating at high flow rates. Unfortunately, to the best of our knowledge, there are no non-linear studies which can accurately account for the whipping instabilities. One way to extend the current analysis is performing a three-dimensional numerical simulations for the highly electrified jets, to predict the critical operational parameters when the whipping instability is initiated along with predicting the droplet size/charge distributions under whipping conditions.

Bibliography

[1] J. M. López-Herrera and A. M. Gañán-Calvo. A note on charged capillary jet breakup of conducting liquids: experimental validation of a viscous one-dimensional model. *J. Fluid Mech.*, 501:303–326, 2004.

[2] J. Zeleny. Instability of electrified liquid surfaces. *Phys. Rev.*, 10:1–16, 1917.

[3] M. Cloupeau and B. Prunet-Foch. Electrostatic spraying of liquids in cone-jet mode. *J. Electrostatics*, 22:135–159, 1989.

[4] L. De Juan and J. Fernandez de la Mora. Charge and size distributions of electrospray drops. *J. Colloid Interface Sci.*, pages 280–293, 1997a.

[5] M. Gamero-Castaño and V. Hurby. Electric measurements of charged sprays emitted by cone-jets. *J. Fluid Mech.*, 459:245–276, 2002.

[6] A.M. Gañán-Calvo, J.M. López-Herrera, M.A. Herrada, A. Ramos, and J.M. Montanero. Review on the physics of electrospray: from electrokinetics to the operating conditions of single and coaxial taylor cone-jets, and ac electrospray. *J. Aerosol. Sci*, 125:32–56, 2018.

[7] J. Rosell-Llompart, J. Grifoll, and I.G. Loscertales. Electrosprays in the cone-jet mode: from taylor cone formation to spray development. *J. Aerosol Sci.*, 125:2–31, 2018.

[8] A. B. Basset. Waves and jets in a viscous liquid. *Am. J. Maths*, 16:93–110, 1894.

[9] J. R. Melcher. Field-coupled surface waves. *MIT Press*, 1963.

[10] D. A. Saville. Stability of electrically charged viscous cylinders. *Phys. Fluids*, 14(6): 1095–1099, 1971.

[11] A.L. Yarin, W. Kataphinan, and D.H. Reneker. Branching in electrospinning of nanofibers. *J. Appl. Phys.*, 98, 2005.

[12] A.J. Mestel. Electrohydrodynamic stability of a slightly viscous jet. *J. Fluid Mech.*, 274:93–113, 1994.

[13] A.J. Mestel. Electrohydrodynamic stability of a highly viscous jet. *J. Fluid Mech.*, 312: 311–326, 1996.

[14] J. M. López-Herrera, Riesco-Chueca P., and A. M. Gañán-Calvo. Linear stability analysis of axisymmetric perturbations in imperfectly conducting liquid jets. *Phys. Fluids.*, 17, 2005.

[15] Q. Wang. Breakup of a poorly conducting liquid thread subject to a radial electric field at zero reynolds number. *Phys. Fluids*, 24(10), 2012.

[16] E. R. Setiawan and S. D. Heister. Nonlinear modeling of an infinite electrified jet. *J. Elec-trostatics*, 42:243–257, 1997.

[17] J. M. López-Herrera, A. M. Gañán-Calvo, and M. Perez-Saborid. One-dimensional simulation of the breakup of capillary jets of conducting liquids. application to e.h.d. spraying. *J. Aerosol Sci.*, 30:895–912, 1999.

[18] H.C. Lee. Drop formation in liquid jets. *IBM J. Res. Develop.*, 18:364–369, 1974.

[19] R. T. Collins, M. T. Harris, and O. A. Basaran. Breakup of electrified jets. *J. Fluid Mech*, 588:75–129, 2007.

[20] L. Rayleigh. On the equilibrium of liquid conducting masses charged with electricity. *Phil. Mag.*, 14:184–186, 1882.

[21] J. R. Lister and H. A. Stone. Capillary breakup of a viscous thread surrounded by another viscous fluid. *Phys. Fluids*, 10:2758–2764, 1998.

[22] R. V. Craster, O. Matar, and D. T. Papageorgiou. On compound threads with large viscosity contrast. *J. Fluid Mech*, 533:95–124, 2005.

[23] Q. Wang and D.T. Papageorgiou. Dynamics of a viscous thread surrounded by anotherviscous fluid in a cylindrical tube under the action of radial electric fields: breakup and touchdown singularities. *J. Fluid Mech.*, 683:27–56, 2011.

[24] Q. Nie, F. Li, Q. Ma, H. Fang, and Z. Yin. Effects of charge relaxation on the electrohydrodynamic breakup of leaky-dielectric jets. *J. Fluid Mech.*, 925, 2021.

[25] F. Li, X.Y. Yin, and X.Z Yin. Small-amplitude shape oscillation and linear instability of an electrically charged viscoelastic liquid droplet. *J. Non-Newtonian Fluid Mech.*, 264:85–97, 2019.

[26] C. Eck, M. Fontelos, G. Grün, F. Klingbeil, and O. Vantzos. On a phase-field model for electrowetting. *Interfaces Free Bound*, 11(2), 2009.

[27] A. M. Lakdawala, A. Sharma, and R. Thaokar. A dual grid level set method based study on similarity and difference bewteen interface dynamics for surface tension and radial electric field induced jet breakup. *Chem. Engng Sci.*, 148:238–255, 2016.

[28] J. M. López-Herrera, A. M. Gañán-Calvo, S. Popinet, and M. A. Herrada. Electrokinetic effects in the breakup of electrified jets: a volume-of-fluid numerical study. *Intl J. Multiphase Flow*, 71:14–22, 2015.

[29] M. Tjahjadi, H. A. Stone, and J. M. Ottino. Satellite and subsatellite formation in capillary breakup.nonlinear modeling of an infinite electrified jet. *J. Fluid Mech.*, 243: 297–317, 1992.

[30] C. F. Brasz, A. Berny, and J. C. Bird. Threshold for discretely self-similar satellite drop formation from a retracting liquid cone. *Phys. Rev. Fluids*, 3:10, 2018.

[31] M. Gamero-Castaño and A. Cisquella-Serra. Electrosprays of highly conducting liquids: A study of droplet and ion emission based on retarding potential and time-of-flight spectrometry. *Phys. Rev. Fluids*, 6(1), 2020.

[32] S.W. Miller, J.R. Ulibarri-Sanchez, B.D. Prince, and R.J. Bemish. Capillary ionic liquid electrospray: beam compositional analysis by orthogonal time-of-flight mass spectrometry. *J. Fluid Mech.*, 928, 2021.

[33] D. Saville. Electrohydrodynamics: the taylor-melcher leaky dielectric model. *Annual review of fluid mechanics*, 29(1), 1997.

[34] A.M. Gañán-Calvo. Cone-jet analytical extension of taylor's electro-static solution and the asymptotic universal scaling laws in electrospraying. *Phys. Rev. Lett.*, 79:217–220, 1997.

[35] A.M. Gañán-Calvo. On the general scaling theory for electrospraying. *J. Fluid Mech.*, 507:203–212, 2004.

[36] J. Eggers and E. Villermaux. Physics of liquid jets. *Rep. Prog. Phys.*, 71:36601, 2008.

[37] S. Chandrasekhar. Hydrodynamic and hydromagnetic stability. *Courier Corporation*, 1981.

[38] G. B. Anderson, D. M. amd Mcfadden and A. A. Wheeler. Diffuse-interface methods in fluid mechanics. *Annu. Rev. Fluid Mech.*, 30:139–165, 1998.

[39] D. Jacqmin. Calculation of two-phase navier–stokes flows using phase-field modelling. *J. Comput. Phys.*, 155:96–127, 1999.

[40] P. Yue, J.J. Feng, C. Liu, and J. Shen. A diffuse-interface method for simulating two-phase flows of complex fluids. *J. Fluid Mech.*, 515:293–317, 2004.

[41] J.M. López-Herrera, Popinet S., and M.A. Herrada. A charge-conservative approach for simulating electrohydrodynamic two-phase flows using volume-of-fluid. *J. Comput. Phys.*, 230:1939–1955, 2011.

[42] G. Tomar, D, Gerlach, G. Biswas, N. Alleborn, A. Sharma, F. Durst, S.W.J. Welch, and A. Delgado. Two-phase electrohydrodynamic simulations using a volume-of-fluid approach. *J. Comput. Phys.*, 227(2):1267–1285, 2007.

[43] I. Roghair, M. Musterd, D. Ende, C. Kleijin, M. Kruetzer, and F. Mugele. A numerical technique to simulate display pixels based on electrowetting. *Microfluidics and Nanofluidics*, 19:465–482, 2015.

[44] L.D. Landau, J.S. Bell, M.J. Kearsley, L.P. Pitaevskii, E.M. Lifshitz, and J.B. Sykes. Electrodynamics of continuous media. *Elsevier*, 8, 2013.

[45] S. Mandal, U. Ghosh, A. Bandopadhyay, and S. Chakraborty. Electro-osmosis of superimposed fluids in the presence of modulated charged surfaces in narrow confinements. *J. Fluid Mech.*, 776, 2015.

[46] H. Ding, M.N. Gilani, and P.D. Spelt. Sliding, pinch-off and detachment of a droplet on a wall in shear flow. *J. Fluid Mech.*, 644, 2010.

[47] M. Gamero-Castaño and M. Magnani. Numerical simulation of electrospraying in the cone-jet mode. *J. Fluid. Mech.*, 859:247–267, 2019.

[48] M. Gamero-Castaño. The structure of electrospray beams in vacuum. *J. Fluid. Mech.*, 604:339–368, 2008.

[49] D. T. Papageorgiou. On the breakup of viscous-liquid threads. *Phys. Fluids*, 7:1529–1544, 1995.

[50] W. Yang, H. Duan, C. Li, and W. Deng. Crossover of varicose and whipping instabilities in electrified microjets. *Physical review letters*, 112(5), 2014.

Appendix A

Role of outer electrode and charge conservation

We test the role of the position of the outer grounded electrode on the dynamics of the deformation and breakup of the electrified jet. For all the simulation results reported in the current article, the outer grounded electrode is located such that $R_e = 12$. Without changing other parameters we run tests by locating the outer electrode such that $R_e = 80$. Figure A.1 depicts the profile of the deformation and breakup of the jet for $Oh = 10$, $\Gamma = 2$ and $k = 0.9$ for the two electrode positions. The profiles of the jet are superimposed on one-another for the same time t. From figure A.1 we can deduce that the electrode at $R_e = 12$ is sufficiently far for this parameter to have a negligible effect on the solution. Note that the electric field on the surface of the nominal jet does not depend on the position of the electrode, because we are fixing the Taylor number by fixing the volumetric charge density in the jet. Provided that the outer electrode is sufficiently far away from the jet, the exact position does not have an effect on the dynamics of the breakup.

The initial dimensional volumetric charge in the jet is calculated with the imposed Taylor

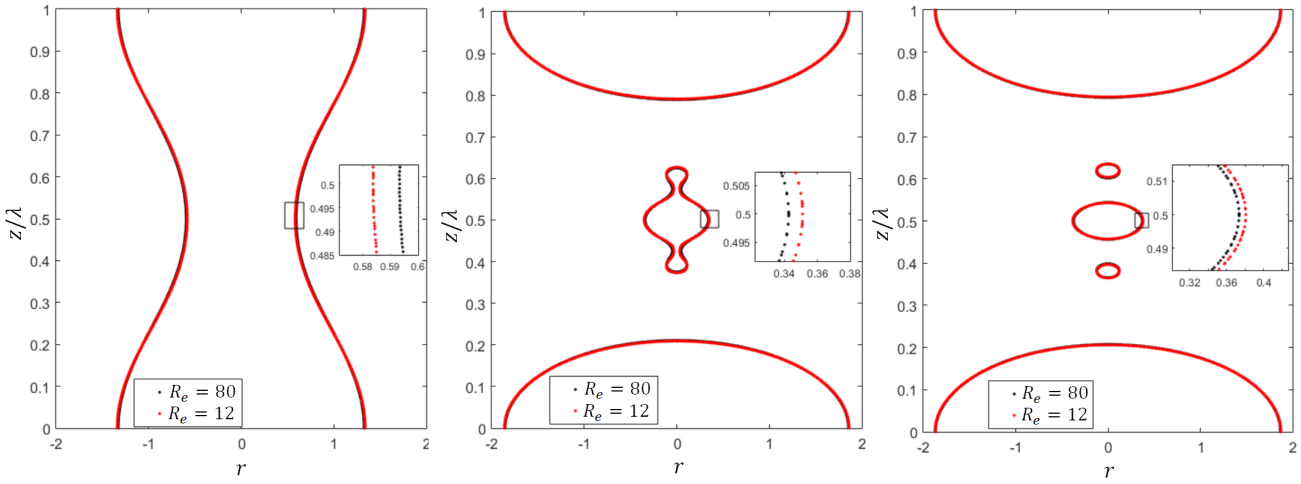

Figure A.1: Comparison between the profile of the interface of the jet for $\Gamma = 2$, $Oh = 10$ and $k = 0.9$ when the grounded electrode is placed far away from the jet ($R_e = 80$) and when $R_e = 12$.

number. For the surface of a cylinder with surface charge density σ, the dimensional electric field on the surface of the cylinder is given as:

$$E(R_j) = \frac{\sigma}{\varepsilon_o} \tag{A.1}$$

Therefore, the dimensional surface charge density is obtained from the Taylor number as:

$$\sigma = \sqrt{\frac{\Gamma \varepsilon_o \gamma}{R_j}} \tag{A.2}$$

We subsequently obtain the initial volumetric charge density ρ_{eo} from the surface charge density as $\rho_{eo} = 2\sigma_e/R_j$. The dimensionless initial volumetric charge density therefore is $\rho_{eo} = 2$. ρ_{eo} is initially distributed uniformly in the domain $0 < r < 1 + Acos(kz)$ at $t < 0$. Since the electrical conductivity of the jet (fluid 2) is much higher than the outside passive medium (fluid 1). The charges relax along the mean interface at $t = 0$. At $t = 0$, the electric field variation along the radial direction could be analytically approximated by the

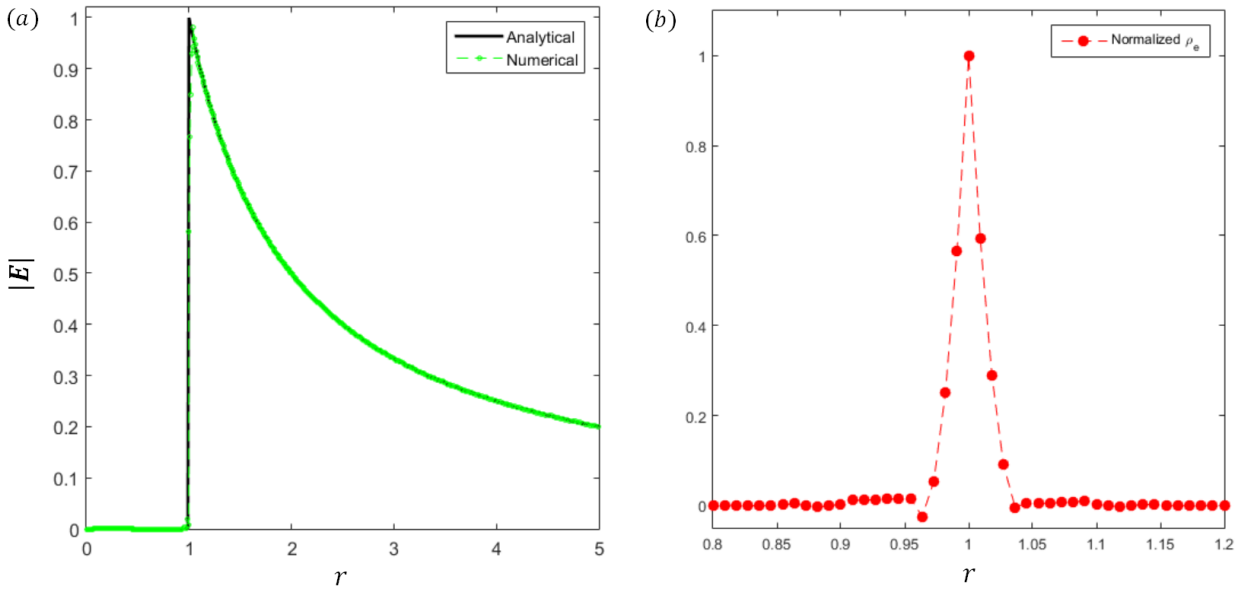

Figure A.2: (a) Electric field variation along the radial direction after the charge relaxation process (at $t = 0$) predicted using the phase-field model and it's comparison with the analytical expression. (b) normalized volumetric charge density along the mean interface at $t = 0$.

expression of electric field variation of a perfectly conducting cylinder, given as:

$$\left.\begin{aligned} |\boldsymbol{E}(r < 1)| &= 0; \\ |\boldsymbol{E}(r \geq 1)| &= \frac{1}{r} \end{aligned}\right\} \tag{A.3}$$

Figure A.2 depicts the electric field variation along the radial direction predicted using the phase-field model after the charges have relaxed along the mean-interface at $t = 0$ and it's comparison with the analytical expression A.3. Since the phase field method is continuous interface method, the electric field in the proximity of $r = 1$ has a continuous and finite slope, however, it compares well with the analytical expression. Figure A.2 (b) depicts the normalized volumetric charge density.

Since, we apply periodic boundary condition in the domain of the simulation at $z = 0$ and $z = \lambda$, the total charges along one wavelength of the jet should be conserved. Figure A.3 depicts the total charge variation in the entire simulation geometry for different cases. Figure

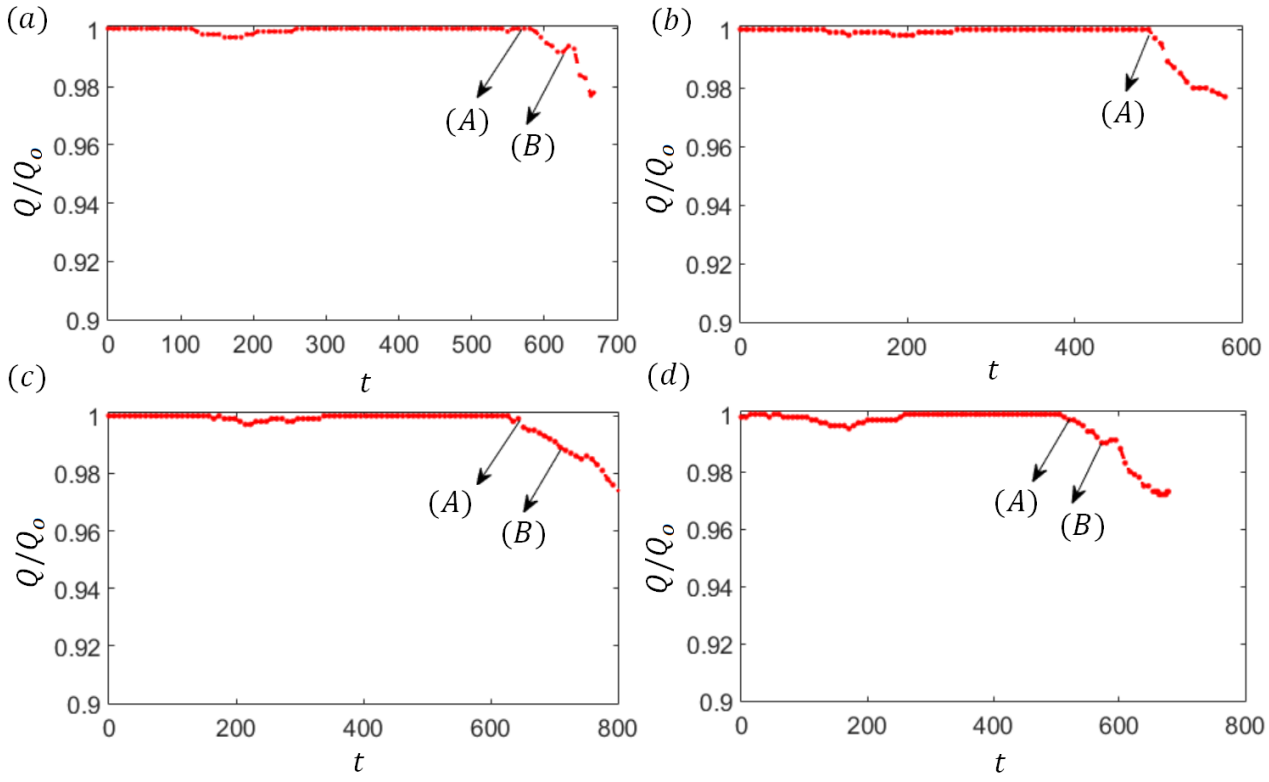

Figure A.3: The total charge in the simulation domain normalized by the initial total charge for different time instants during the deformation-breakup process. (A) refers to the time instant when the size and charges of the primary and satellite droplet is made. (B) refers to the time instant when the size and charges are measured for sub-satellite droplets. Figure (a) $k = 0.6$, $\Gamma = 2$, $Oh = 10$, (b) $k = 1$, $\Gamma = 2$, $Oh = 10$, (c) $k = 0.6$, $\Gamma = 3$, $Oh = 10$, (d) $k = 0.7$, $\Gamma = 3$, $Oh = 10$.

A.3(a) depicts the total charge variation for $Oh = 10$, $\Gamma = 2$ and $k = 0.6$, the arrows (A) and (B) depict the time instant at which the charges on the droplets are calculated (right after respective pinch-off). After pinch-off there is a loss in the total charge in the geometry. However, since we are only limited to measuring the charges just after each pinch-off process. The charges measured are within a $1 - 1.7\%$ error range and hence the present setup along with the numerical validation with prior experimental results gives us confidence in our numerical measurements. However, after the formation of primary, satellite and sub-satellite droplets we cannot capture the Rayleigh instability process of the droplets which are above the Rayleigh limit, as the charges fail to be conserved in our simulation domain for extended periods after break-up.